J. Fluid Mech. (2002), *vol.* 464, *pp.* 165–207.
DOI: 10.1017/S0022112002008789 Printed in the United Kingdom

Emergence of intense jets and Jupiter's Great Red Spot as maximum-entropy structures

By F. BOUCHET[1] AND J. SOMMERIA[2]

[1]UMR 5582, Institut Fourier, BP 74, 38402 Saint Martin d'Hères Cedex, France

[2]CNRS, LEGI/Coriolis, 21 av. des Martyrs, 38 000 Grenoble, France

(Received 13 March 2000 and in revised form 14 January 2002)

We explain the emergence and robustness of intense jets in highly turbulent planetary atmospheres, like that on Jupiter, by a general statistical mechanics approach to potential vorticity patches. The idea is that potential vorticity mixing leads to the formation of a steady organized coarse-grained flow, corresponding to the statistical equilibrium state. Our starting point is the quasi-geostrophic 1-1/2 layer model, and we consider the relevant limit of a small Rossby radius of deformation. Then narrow jets are obtained, in the sense that they scale like the radius of deformation. These jets can be either zonal, or closed into a ring bounding a vortex. Taking into account the beta-effect and a sublayer deep shear flow, we predict organization of the turbulent atmospheric layer into an oval-shaped vortex within a background shear. Such an isolated vortex is centred over an extremum of the equivalent topography, combining the interfacial geostrophic tilt due to the deep shear flow and the planetary beta-effect (the resulting effective beta-effect is locally quadratic). This prediction is in agreement with an analysis of wind data in major Jovian vortices (Great Red Spot and Oval BC).

1. Introduction

Atmospheric and oceanic flows are often organized into narrow jets. They can flow zonally around the planet like the jet streams in the Earth's stratosphere, or the eastward jet at 24° latitude in the northern hemisphere of Jupiter (Maxworthy 1984). Jets can alternatively become organized into rings, forming vortices, like the rings shed by the meandering of the Gulf-Stream in the western Atlantic Ocean. The flow field in Jupiter's most famous feature, the Great Red Spot, is an oval-shaped jet, rotating in the anticyclonic direction and surrounding an interior area with a weak mean flow (Dowling & Ingersoll 1989), see figure 1(*a*). It is located at the same latitude as the above-mentioned eastward jet, but in the southern hemisphere. Robust cyclonic vortices are also observed with a similar jet structure (Hatzes *et al.* 1981), see figure 1(*b*).

Such jets and vortices are in turbulent surroundings, and the persistence of their strength and concentration in the presence of eddy mixing is intriguing. The explanation proposed in this paper is based on a statistical mechanical approach: the narrow jet or vortex appears as the most probable state of the flow after the turbulent mixing of potential vorticity, taking into account constraints due to the quantities conserved by the dynamics, especially energy. Such a statistical theory has been first proposed for the two-dimensional Euler equations by Kuz'min (1982), Robert (1990), Robert & Sommeria (1991), Miller (1990), see Sommeria (2001) for a recent review.

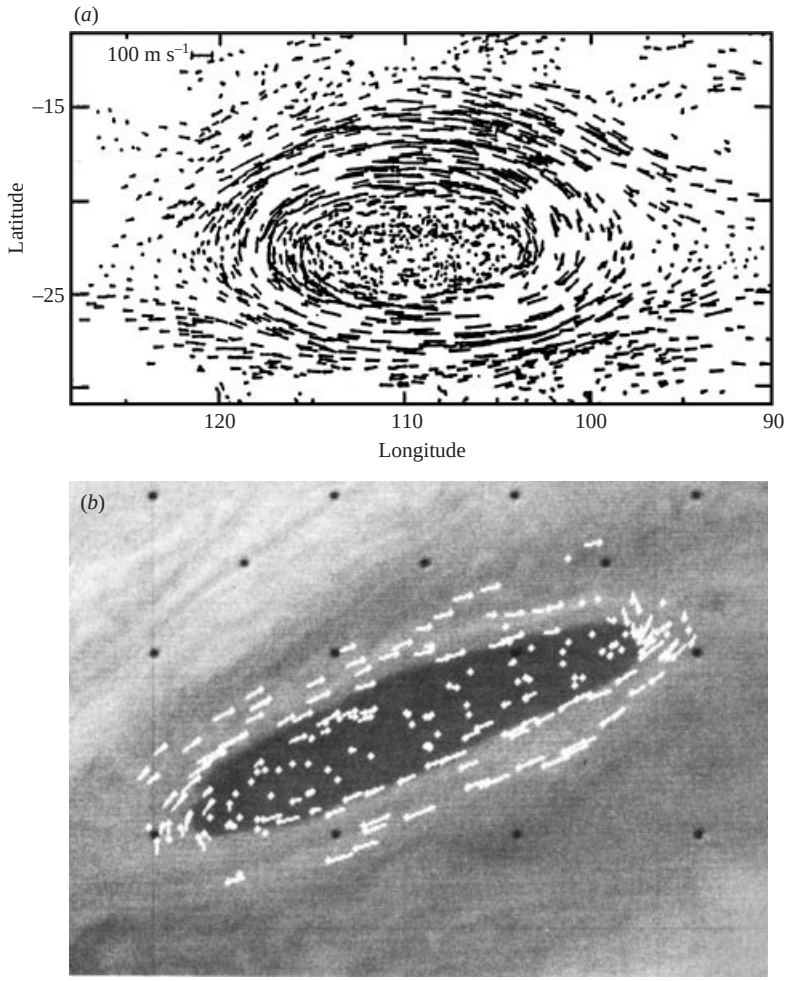

FIGURE 1. Annular jets observed in the atmosphere of Jupiter. (*a*) Velocity field in the Great Red Spot of Jupiter (20° S), from Dowling & Ingersoll (1988). (*b*) Velocity field in the cyclonic Barge of Jupiter (14° N) from Hatzes *et al.* (1981).

This theory predicts the organization of two-dimensional turbulence into a steady flow, superposed with fine-scale 'microscopic' vorticity fluctuations. This is by far the most likely result of random stirring, so the evolution to this statistical equilibrium is in practice irreversible, although it is not at the molecular level (in a second stage, true molecular mixing can suppress the local fluctuations, but without influencing the mean flow). Complete vorticity mixing is prevented by the conservation of the energy, which can be expressed as a constraint in the accessible vorticity fields. A similar, but quantitatively different, organization had been previously obtained with statistical mechanics of singular point vortices with the mean field approximation, instead of continuous vorticity fields (Onsager 1949; Joyce & Montgomery 1973). The possibility of using such ideas to explain the Great Red Spot has been suggested since the first works on the two-dimensional Euler statistical mechanics by Robert (1990), Miller (1990), Sommeria *et al.* (1991*a*) and Miller, Weichman & Cross (1992), but without explicit predictions.

A first step in this direction has been the extension to the quasi-geostrophic (QG)

model, discussed by Sommeria *et al.* (1991*a*), Michel & Robert (1994*a*) and Kazantsev, Sommeria & Verron (1998). The QG model describes a shallow water system with a weak vorticity in comparison with the planetary vorticity (small Rossby number), such that the flow is in geostrophic balance, and the corresponding free-surface deformation is supposed small in comparison with the layer thickness. The new contribution of the present work is to provide explicit predictions in the frame of a realistic model for the Jovian atmosphere, proposed by Dowling & Ingersoll (1989), see also Dowling (1995). The free surface of this shallow water system represents the bottom of the active atmospheric layer, floating on a denser fluid with a given deep zonal flow, depending only on latitude. The gradient of planetary vorticity is accounted for by a beta-effect. An additional beta-effect, depending on the latitude coordinate y, is introduced to represent the influence of the deep zonal flow on the active layer, through the geostrophic tilt of the interface. Dowling & Ingersoll (1989) found organization into a single vortex from direct numerical computations. Our analytical approach provides a broader understanding of the general conditions for such a self-organization process. We find for instance that a small change in a bifurcation parameter yields an intense zonal jet, as observed in the northern hemisphere.

The free-surface deformability, representing the strength of the density stratification, is controlled by the Rossby radius of deformation R^*. The two-dimensional Euler equation is recovered in the limit of very strong stratification for which $R^* \to \infty$. We consider in this paper the opposite limit of weak stratification for which R^* is much smaller than the scale of the system L. This limit is appropriate for large-scale oceanic currents, as the radius of deformation is typically 10–100 km. For Jupiter, R^* is estimated to be in the range 500–2500 km, while the Great Red Spot extends over 20 000 km in longitude, and 10 000 km in latitude, so the limit $R^*/L \to 0$ seems relevant. We show that in this limit the statistical equilibrium is made up of quiescent zones with well-mixed uniform potential vorticity, bounded by jets with thickness of order R^* and jet velocity diverging in R^{*-1}. The persistence of such intense jets is therefore justified as the result of turbulence mixing. Some of the ideas used have been already sketched in Sommeria *et al.* (1991*a*), but we here provide a systematic derivation and thorough analysis.

The QG approximation is thought to break down for scales much larger than the radius of deformation, so that the limit $R^*/L \to 0$ seems inconsistent with this approximation. However the relevant scale is the jet width, which remains of order R^*, so that the QG approximation does remain valid in this limit. This point has been discussed by Marcus (1993) for the Great Red Spot, which he supposes to be a uniform-potential-vorticity (PV) spot surrounded by a uniform-PV background (we here justify this structure as the result of PV mixing with constraints on the conserved quantities). Analysing wind data in the Great Red Spot, Dowling & Ingersoll (1989) concluded that the QG approximation is good within typically 30% error, which is reasonable to a first approximation. Statistical mechanics of the more general shallow water system (Chavanis & Sommeria 2002), predicts a similar jet structure. The present QG results therefore provide a good description as a first approximation.

We first consider the case without beta-effect in § 2, and furthermore assume periodic boundary conditions (along both coordinates) to avoid consideration of boundary effects. Starting from some initial condition with patches of uniform PV, we find that these patches mix with uniform density (probability) in two subdomains, with strong density gradient at the interface, corresponding to a free jet. The coexistence of the two sub-domains can be interpreted as an equilibrium between two thermodynamic

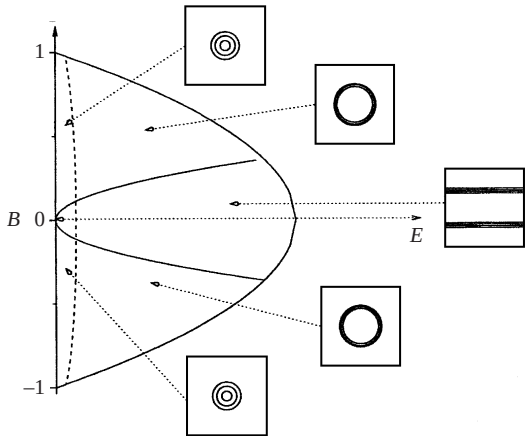

FIGURE 2. Phase diagram of the Gibbs states versus the energy E and the asymmetry parameter B representing the normalized initial areas of the PV level a_1 (see definition in § 2.2.1). The outer solid line is the maximum energy achievable for a fixed B: $E = \frac{1}{2}R^2(1 - B^2)$. Straight jets are obtained for the nearly symmetric cases ($B \approx 0$), while a vortex is formed when one of the PV levels has a lower area. This vortex takes the form of a circular jet for sufficiently high energy. This plot is derived in § 2.3.3. The boundary line between the straight jets and the circular jet corresponds to a vortex area $A_1 = 1/\pi$ or $A_{-1} = 1/\pi$ and its energy has been calculated using (33) and (34): $E = R^2B^2(2\pi - 2)/(\pi - 2)^2$. The dotted line representing the boundary between the axisymmetric vortex and circular jet is defined as the energy value for which vortex area A_1 or A_{-1} (33) is equal to $(2l)^2$, where l is the typical jets width (figure 7). This line depends on the value of R, the ratio of the Rossby deformation radius to the domain scale. Here, it has been numerically calculated for $R = 0.03$.

phases. We find that the interface has a free energy per unit of length, and its minimization leads to a minimum length at equilibrium. This results in a constant radius of curvature, in analogy with surface tension effects in thermodynamics, leading to spherical bubbles or droplets. The range of the vortex interaction is of the order R^*, therefore becoming very small in the limit of small radius of deformation, so the statistical equilibrium indeed behaves as in usual thermodynamics with short-range molecular interactions. This contrasts with the case of the Euler equation, with long-range vortex interactions, analogous to gravitational effects (Chavanis, Sommeria & Robert 1996; Chavanis 1998).

Figure 2 summarizes the calculated equilibrium states in this periodic case, depending on the total energy and a parameter B representing the asymmetry between the initial PV patch areas, before the mixing process. We obtain a pair of straight jets (with opposite direction) for a weak asymmetry and a circular jet otherwise. Such a circular jet reduces to an axisymmetric vortex, with radius of order R^*, in the limit of low energy.

The influence of the beta-effect or the deep zonal flow modifies the shape of these jets, as discussed in § 3. The channel geometry, representing a zonal band periodic in the longitude x is appropriate for that study. With the usual beta-effect βy, linear in the transverse coordinate y, statistical equilibrium is, depending on the initial parameters, a zonal flow or a meandering eastward jet or a uniform velocity $v_m = R^2\beta$ whose induced free-surface slope cancels the beta-effect (uniformization of PV) on which circular vortices can coexist.

For more general beta-effects, due to the deep zonal flow, we find that the jet curvature depends on latitude y. In particular a quadratic beta-effect ay^2 leads to statistical

equilibrium states with oval-shaped jets, similar to the Great Red Spot. Moreover, the latitude of the vortex centre is the extremum of the beta-effect (determined in the vortex reference frame). Using the determination of the sublayer flow from Voyager data by Dowling & Ingersoll (1989), we show in § 4, that such a quadratic beta-effect is indeed a realistic model for Jupiter's atmosphere in the latitude range of the Great Red Spot and the White Ovals, the other major coherent vortices on Jupiter (recently merged into a single vortex). We finally propose an explicit model which, starting from random PV patches, predicts the organization into either an oval-shaped vortex or zonal jets, depending on the energy and the asymmetry parameter.

2. The case with periodic boundary conditions

2.1. *The dynamical system*

We start from the barotropic quasi-geostrophic (QG) equation:

$$\frac{\partial q}{\partial t} + \boldsymbol{v} \cdot \nabla q = 0, \tag{1}$$

$$q = -\Delta\psi + \frac{\psi}{R^2} - h(y), \tag{2}$$

$$\boldsymbol{v} = -\boldsymbol{e}_z \wedge \nabla\psi, \tag{3}$$

where q is the potential vorticity (PV), advected by the non-divergent velocity $\boldsymbol{v}$, ψ is the stream function,† R is the internal Rossby deformation radius between the layer of fluid under consideration and a deep layer unaffected by the dynamics; x and y are respectively the zonal and meridional coordinates (x is directed eastward and y northward). The term $h(y)$ represents the combined effect of the planetary vorticity gradient and of a given stationary zonal flow in the deep layer, with stream function $\psi_d(y)$: $h(y) = -\beta y + \psi_d/R^2$. This deep flow induces a constant deformation of the free-surface, acting like topography on the active layer.‡ We shall therefore call $h(y)$ the 'topography', and study its influence in § 3. Let us assume $h(y) = 0$ in this section. We define the QG equations (1), (2) in the non-dimensional square $D = [-\frac{1}{2}, \frac{1}{2}]^2$. R is then the ratio of the internal Rossby deformation radius R^* to the physical scale of the domain L.

Let $\langle f \rangle \equiv \int_D f \, \mathrm{d}^2\boldsymbol{r}$ be the average of f on D for any function f. Physically, as the stream function ψ is related to the geostrophic pressure, $\langle\psi\rangle$ is proportional to the mean height at the interface between the fluid layer and the bottom layer, and due to the mass conservation it must be constant (Pedlosky 1987). We make the choice

$$\langle\psi\rangle = 0 \tag{4}$$

without loss of generality.

† We choose for the stream function ψ the standard sign convention used for the Euler equation, which is the opposite of the one commonly used in geophysical fluid dynamics. Our stream function ψ is therefore proportional to the opposite of the pressure fluctuation in the northern hemisphere and to the pressure fluctuation in the southern hemisphere, as the planetary vorticity sign is reversed. The signs of q and $\boldsymbol{v}$ are not influenced by this choice of sign for ψ.

‡ A real topography $\eta(y)$ would correspond to $h(y) = -f_0\eta(y)/h_0$ where f_0 is the reference planetary vorticity at the latitude under consideration and h_0 is the mean upper layer thickness. Due to the sign of f_0, the signs of h and η would be the same in the southern hemisphere and opposite in the northern hemisphere. As we will discuss the Jovian southern hemisphere vortices extensively, we have chosen this sign convention for h.

The total circulation is $\langle q \rangle = \langle -\Delta\psi + \psi/R^2 \rangle = \langle \psi/R^2 \rangle$ due to the periodic boundary conditions. Therefore

$$\langle q \rangle = 0. \tag{5}$$

We note that the Dirichlet problem (2) on D with periodic boundary conditions has a unique solution ψ for a given PV field.

Due to the periodic conditions for ψ, the linear momentum is also equal to 0,

$$\langle \boldsymbol{v} \rangle = 0. \tag{6}$$

The energy

$$E = \frac{1}{2}\int_D q\psi \, \mathrm{d}^2\boldsymbol{r} = \frac{1}{2}\int_D \left[(\nabla\psi)^2 + \frac{\psi^2}{R^2}\right] \mathrm{d}^2\boldsymbol{r} \tag{7}$$

is conserved (we note that the first term on the right-hand side of (7) is the kinetic energy whereas the second one is the gravitational available potential energy).

The Casimir integrals

$$C_f(q) = \int_D f(q) \, \mathrm{d}^2\boldsymbol{r} \tag{8}$$

for any continuous function f are also conserved, and in particular the different moments of the PV. Their conservation, as well as energy conservation, is a consequence of symmetries of the Hamiltonian structure from which the QG equations (1), (2) may be derived (see Salmon 1988 or Shepherd 1990 for reviews on Hamiltonian formalism in the context of geophysical fluid dynamics).

2.2. *The statistical mechanics on a two-PV-level configuration*

2.2.1. *The macroscopic description*

The QG equations (1) and (2) are known to develop very complex vorticity filaments. Because of the rapidly increasing amount of information it would require, as time increases, a deterministic description of the flow for long time is both unrealistic and meaningless. The statistical theory adopts a probabilistic description for the vorticity field. The statistical equilibrium depends on the energy and on the global probability distribution of PV levels. We shall consider the most simple case with only two PV levels. As discussed in § 4, incoming thermal plumes should form patches with high anticyclonic PV in a more quiet background, a situation which can be reasonably described with two PV levels (high and low) in the absence of more information about the forcing. Generalization to more PV levels is straightforward in principle but it would involve more unknown parameters to describe the distribution of PV areas. We expect only minor differences with the two-level case, as suggested by various previous studies of the equilibrium states for two-dimensional Euler statistical mechanics (Sommeria *et al.* 1991; Chen & Cross 1996; Kazantsev *et al.* 1998): the equilibrium state is only weakly dependent on the discretization in vorticity levels.

The determination of the statistical equilibrium then depends only on the energy E, on the two PV levels, denoted $q = a_1$ and $q = a_{-1}$ and on their respective areas A and $(1 - A)$ in D (the conservation of these areas is then equivalent to the conservation of all the Casimirs (8)). The number of free parameters can be further reduced by appropriate scaling. Indeed a change in the time unit permits the PV levels to be defined up to a multiplicative constant, and we choose for the sake of simplicity

$$\frac{a_1 - a_{-1}}{2} = 1 \tag{9}$$

and define the non-dimensional parameter B as

$$B \equiv \frac{a_1 + a_{-1}}{2}. \tag{10}$$

The condition (5) of zero mean PV imposes that $a_1 A + a_{-1}(1 - A) = 0$. This means that a_1 and a_{-1} must be of opposite sign and, using (9) and (10), $A = (1 - B)/2$. The distribution of PV levels is therefore fully characterized by the single asymmetry parameter B, which takes values between -1 and $+1$. The symmetric case of two PV patches with equal area $A = 1/2$ corresponds to $B = 0$, while the case of a patch with small area (but high PV, such that $\langle q \rangle = 0$) corresponds to $B \to 1$. Note that we can restrict the discussion to $B \geqslant 1$ as the QG system is symmetric for a change of sign of the PV.

The two PV levels mix due to turbulent effects, and the resulting state is locally described by the local probability (local area proportion) $p(\boldsymbol{r})$ to find the first level at the location $\boldsymbol{r}$. The probability of finding the complementary PV level a_{-1} is $1 - p$, and the locally averaged PV at each point is then

$$\bar{q}(\boldsymbol{r}) = a_1 p(\boldsymbol{r}) + a_{-1}(1 - p(\boldsymbol{r})) = 2(p - \tfrac{1}{2}) + B, \tag{11}$$

where the second relation is obtained by using (9) and (10).

Since the patch with PV level a_1 is mixed but globally conserved, the integral of its density p over the domain must be equal to the initial area A,

$$A \equiv \frac{1 - B}{2} = \int_D p(\boldsymbol{r})\, \mathrm{d}^2\boldsymbol{r}. \tag{12}$$

As the effect of local PV fluctuations is filtered out by integration ($\bar{\psi} = \psi$ and $\bar{\boldsymbol{v}} = \boldsymbol{v}$), the stream function and the velocity field are fully determined by the locally averaged PV $\bar{q}$ as the solution of

$$\bar{q} = -\Delta\psi + \frac{\psi}{R^2}, \quad \psi \quad \text{periodic} \tag{13}$$

and

$$\boldsymbol{v} = -\boldsymbol{e}_z \wedge \nabla\psi.$$

Therefore the energy is also expressed in terms of the field $\bar{q}$:

$$E = \frac{1}{2}\int_D \left[(\nabla\psi)^2 + \frac{\psi^2}{R^2}\right] \mathrm{d}^2\boldsymbol{r} = \frac{1}{2}\int_D \bar{q}\psi\, \mathrm{d}^2\boldsymbol{r}. \tag{14}$$

Here the energy of the 'microscopic' PV fluctuations has been neglected (replacing q by $\bar{q}$), as justified in the case of Euler equation by Robert & Sommeria (1991). Indeed, for a 'cutoff' for the microscopic fluctuations much smaller than R, the small-scale dynamics coincides with the Euler case.

The central result of the statistical mechanics of the QG equations (1), (2) is that, under an ergodic hypothesis, we expect the long-time dynamics to converge towards the Gibbs states defined by maximizing the mixing entropy

$$S = -\int_D [p(\boldsymbol{r}) \ln p(\boldsymbol{r}) + (1 - p(\boldsymbol{r})) \ln(1 - p(\boldsymbol{r}))]\, \mathrm{d}^2\boldsymbol{r} \tag{15}$$

under the constraints of the global PV distribution (12) and energy (14). It can be shown that the microscopic states satisfying the constraints given by the conservation laws are overwhelmingly concentrated near the Gibbs state, which is therefore likely to be reached after a complex flow evolution. A good justification of this statement is

obtained by the construction of converging sequences of approximations of the QG equations (1), (2), in finite-dimensional vector spaces, for which a Liouville theorem holds. This is a straightforward translation of the work of Robert (2000) for two-dimensional Euler equations. The sequence of such Liouville measures has then the desired concentration properties as (1), (2) enter in the context considered in Michel & Robert (1994*b*).

As in standard statistical mechanics (in gas for instance), the ergodic property of a system is very unlikely to be proven for any generic system (in the current state of our knowledge) and could moreover appear to be wrong in general. A weaker property of mixing is however sufficient to justify the statistical mechanics due to the concentration property stated in the above paragraph. The Gibbs state is most likely to be reached even if the available microscopic states are not evenly explored. In practice, the theory can be validated or invalidated only on the basis of its success or failure to predict well-characterized phenomena. We postpone to the conclusion a critical discussion of statistical mechanics ideas and geophysical applications such as in the Jovian atmosphere.

2.2.2. *The Gibbs states*

Following Robert & Sommeria (1991), we seek maxima of the entropy (15) under the constraints (12) and (14). To account for these constraints, we introduce two corresponding Lagrange multipliers, which we denote 2α and $-C/R^2$ for convenience in future calculations. Then the first variation of the functionals satisfies

$$\delta S - 2\alpha\delta A + \frac{C}{R^2}\delta E = 0$$

for all variations δp of the probability field p. After straightforward differentiation we obtain

$$\left.\begin{aligned} \delta S &= -\int_D [\ln p - \ln(1-p)]\delta p \,\mathrm{d}^2\boldsymbol{r}, \quad \delta A = \int_D \delta p \,\mathrm{d}^2\boldsymbol{r}, \\ \delta E &= \int_D \psi\delta\bar{q} \,\mathrm{d}^2\boldsymbol{r} = \int_D 2\psi\delta p \,\mathrm{d}^2\boldsymbol{r}, \end{aligned}\right\} \tag{16}$$

where the expression for δE has been obtained by integrating by parts and expressing $\bar{q}$ by (11). Then we can write the first in the form $\int_D[-\ln p + \ln(1-p) - 2\alpha + 2C\psi/R^2]\delta p \,\mathrm{d}^2\boldsymbol{r}$, which must vanish for any small variation δp. This implies that the integrand must vanish, and yields the equation for the optimum state:

$$p = \frac{1 - \tanh(\alpha - (C\psi/R^2))}{2}, \tag{17}$$

and using (11) and (13), the partial differential equation

$$q = -\Delta\psi + \frac{\psi}{R^2} = B - \tanh\left(\alpha - \frac{C\psi}{R^2}\right) \tag{18}$$

determining the Gibbs states (statistical equilibrium). From now on we omit the q overbar for the locally averaged PV and refer to it as the PV.

We have shown that for any solution of the variational problem, two constants α and C exist such that ψ satisfies (18). Conversely it can be proved that for any two such constants, a solution to equation (18), in general not unique, always exists. Then p associated with one of these solutions by (17) is a critical point of the 'free energy' $-S(p) + 2\alpha A(p) - (C/R^2)E(p)$ (i.e. its first variation vanishes). Then the Lagrange

multipliers are not given but have to be calculated by prescribing the constraints (12) and (14) corresponding to the two parameters B and E respectively, given by the initial condition. Furthermore, among the states of given energy E and asymmetry parameter B, we have to select the actual free-energy minima (or constrained-entropy maxima).

Finally, let us find a lower bound for the parameter C of the Gibbs states with non-zero energy (i.e. ψ is not uniform). Multiplying (18) by $-\Delta\psi$, integrating by parts and defining $f(C\psi) \equiv B - \tanh(\alpha - (C\psi/R^2))$, we obtain

$$C = \frac{\displaystyle\int_D \left((\Delta\psi)^2 + \frac{1}{R^2}(\nabla\psi)^2 \right) \mathrm{d}^2\boldsymbol{r}}{\displaystyle\int_D -f'(C\psi)(\nabla\psi)^2 \, \mathrm{d}^2\boldsymbol{r}},$$

from which, using $0 < -f'(C\psi) \leqslant 1/R^2$ it follows that when ψ is not constant

$$C > 1. \tag{19}$$

2.3. *The limit of small Rossby deformation radius*

As suggested by oceanographic or Jovian parameters, we seek solutions for the Gibbs state equation in the limit of a small ratio between the Rossby deformation radius and the length scale of the domain: $R \ll 1$ with our non-dimensional coordinates. Then we expect that the Laplacian in the Gibbs state equation (18) can be neglected with respect to ψ/R^2, leading to sub-domains with uniform ψ separated by interfaces, where strong ψ gradients are localized. The sub-domain areas and ψ values will be given by a condition of thermodynamic phase equilibrium, while the contour length will be a minimum, to minimize the free energy.†

2.3.1. *The uniform subdomains*

Neglecting the Laplacian transforms the Gibbs states equation (18) into the algebraic equation:

$$q = \frac{\psi}{R^2} = B - \tanh\left(\alpha - \frac{C\psi}{R^2}\right). \tag{20}$$

Depending on the parameters, this equation has either one or two or three solutions, denoted ψ_{-1}, ψ_0 and ψ_1 in increasing order (see figure 3). The case with a single solution would correspond to a uniform ψ, which should be equal to 0 due to the condition $\langle\psi\rangle = 0$. This is only possible for $E = 0$. Otherwise, we have therefore two or three solutions, with different solutions occurring in subdomains. This condition of multiple solutions requires that the maximum slope for the right-hand side of (20) must be greater than $1/R^2$; this is always realized due to the inequality (19). Furthermore α must be in an interval centred in CB ($\alpha = CB$ in the symmetric case of figure 3).

† Modica (1987) considered the minimization of the functional $E_\epsilon(u) = \int_\Omega [\epsilon(\nabla u)^2 + W_0(u)] \, \mathrm{d}\mathbf{x}$ with the constraint $\int_\Omega u(\mathbf{x}) \, \mathrm{d}\mathbf{x} = m$ in the limit $\epsilon \to 0^+$ where W_0 is a real function with two relative minima. He proved, working with bounded variation functions, that if (u_ϵ) are solutions of this variational problem, for any sub-sequence of (u_ϵ) converging in $L^1(\Omega)$ as $\epsilon \to 0$, this sub-sequence converges to a function u_0 which takes only the values of W_0 at its minima; and the interface between the corresponding subdomains have a minimal area. We note that for a convenient choice of W_0 the corresponding equation for the first-order variations may be the same as the Gibbs state equation (18). However, as the variational problem itself is different, this result cannot be used in our context.

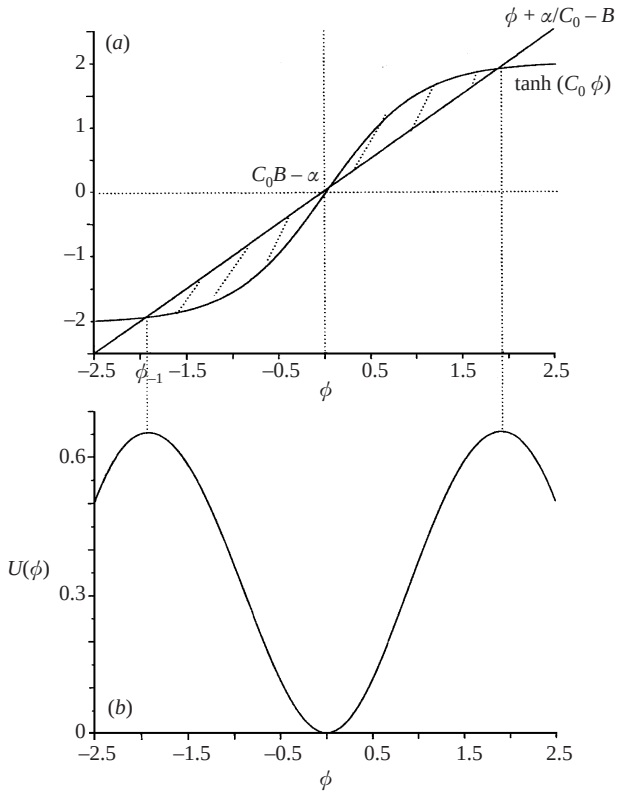

FIGURE 3. (*a*) Graphical representation of the algebraic equation (20), with the rescaled variable $\phi \equiv -\alpha/C + \psi/R^2$. The three solutions are at the intersection of the curve (left-hand side) and straight line (right-hand side). Here the integrability condition $\alpha = C_0 B$ for the differential equation (38) is satisfied, so the two hatched areas are equal. (*b*) The corresponding potential $U(\phi)$, given by (39), the integral from 0 to ϕ of the difference between the two curves (hatched area in *a*).

At the interface between two constant-stream-function subdomains, a strong gradient of ψ necessarily occurs, corresponding to a jet along the interface. These jets make first-order contributions to the entropy and energy, but let us first describe the zero-order problem. Suppose that ψ takes the value ψ_1 (resp. ψ_{-1}) in subdomains of total area A_1 (resp. A_{-1}). The reason why we do not select the value ψ_0 will soon become clear. Using (11) we conclude that the probability p takes two constant values $p_{\pm 1}$ in their respective subdomains. The two areas $A_{\pm 1}$ (measured from the middle of the jet) are complementary such that

$$A_1 + A_{-1} = 1. \tag{21}$$

Furthermore the constraint (4) of zero domain average for ψ implies at zero order

$$\psi_1 A_1 + \psi_{-1} A_{-1} = 0, \tag{22}$$

or equivalently, using $q_{\pm 1} = \psi_{\pm 1}/R^2$, (11) and (21)

$$2A_1(p_1 - \tfrac{1}{2}) + 2(1 - A_1)(p_{-1} - \tfrac{1}{2}) = -B. \tag{23}$$

This can also be obtained from the constraint on the (microscopic) PV patch area (12). The energy inside the subdomains reduces to the potential term $\psi^2/2R^2$, since velocity vanishes. This area energy E_A can be computed in terms of $p_{\pm 1}$ using $q_{\pm 1} = \psi_{\pm 1}/R^2$

and (11):

$$E_A \equiv \frac{\psi_1^2 A_1 + \psi_{-1}^2 A_{-1}}{2R^2} = A_1 e(p_1) + (1 - A_1) e(p_{-1}) \tag{24}$$

with

$$e(p) \equiv R^2(2(p - \tfrac{1}{2})^2 + 2B(p - \tfrac{1}{2}) + \tfrac{1}{2}B^2). \tag{25}$$

There is also energy in the jet at the interface of the subdomains, but it is small with respect to E_A. Indeed the velocity in the jet, of width R, is of order $(\psi_1 - \psi_{-1})/R \sim \psi/R$, and the corresponding integrated kinetic energy is of order ψ^2/R. This is small in comparison with the area energy E_A of order ψ^2/R^2. A precise calculation will confirm this estimate in the next subsection.

We need to determine three unknowns: the area A_1 and the probabilities $p_{\pm 1}$ of the PV level a_1 in each subdomain, while the constraints (23) and (24) provide two relations. An additional relation will be given by entropy maximization. As we neglect the jet area, the entropy reduces at order zero to the area entropy:

$$S_A \equiv A_1 s(p_1) + (1 - A_1) s(p_{-1}) \quad \text{with} \quad s(p) \equiv -p \log p - (1 - p) \log(1 - p). \tag{26}$$

Thus the zero-order problem corresponds to the maximization of the area entropy (26) with respect to the three parameters $p_{\pm 1}$ and A_1, under the two constraints (23) and (24). A necessary condition for a solution of this variational problem is the existence of two Lagrange parameters α_0 and C_0 such that the first variations of the total free energy,

$$F_A \equiv -S_A - \frac{C_0}{R^2} E_A + \alpha_0 \frac{\langle \psi \rangle}{R^2}, \tag{27}$$

vanish. Let us calculate F_A using (23) and (24):

$$F_A = A_1 f(p_1) + (1 - A_1) f(p_{-1}), \tag{28}$$

with

$$f(p) \equiv -s(p) - 2C_0(p - \tfrac{1}{2})^2 - 2(C_0 B - \alpha_0)(p - \tfrac{1}{2}) - \tfrac{1}{2} C_0 B^2 - \alpha_0 B. \tag{29}$$

The vanishing of the variations with respect to p_1 and p_{-1} means that $f(p_{\pm 1})$ are local minima of the free energy $f(p)$. It is easily proven that the function f has two local minima and one local maximum (for $C_0 > 1$ and $C_0 B - \alpha_0$ small enough), see figure 4. The local maximum is achieved for p_0 corresponding to ψ_0. This is why it has not been selected for the uniform subdomains. In addition, the vanishing of the first variations with respect to the area A_1 imposes that the free energies $f(p_{\pm 1})$ in the two subdomains be equal. This is like the condition of thermodynamic equilibrium for a chemical species shared by two coexisting phases.

In the expression (29) for $f(p)$, the entropy term $s(p)$ is symmetric with respect to $p = \frac{1}{2}$, as well as the quadratic term. Therefore if the linear term in $(p - \frac{1}{2})$ vanishes the two maxima are equal, with $p_{\pm 1}$ symmetric with respect to $\frac{1}{2}$. The addition of a linear term obviously breaks this condition of two equal maxima, so the coefficient of the linear term must vanish, thus

$$\alpha_0 = C_0 B. \tag{30}$$

Since $p_{\pm 1}$ are symmetric with respect to $\frac{1}{2}$, we introduce the parameter u as

$$p_{\pm 1} = \tfrac{1}{2}(1 \pm u). \tag{31}$$

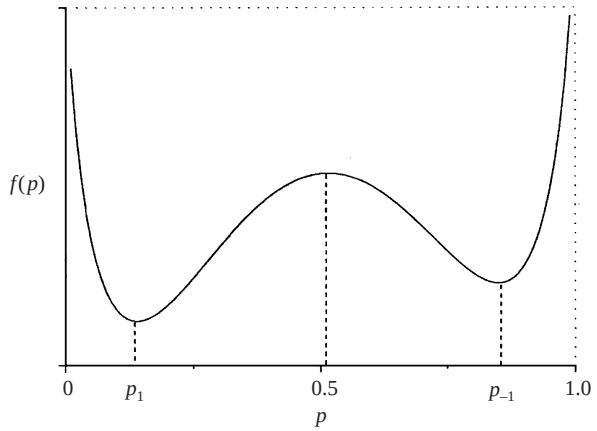

FIGURE 4. The free energy density $f(p)$ (29) versus the probability p. For $C_0 > 1$ and $(C_0B - \alpha_0)$ small enough $f(p)$ has two local minima and one local maximum, allowing two values $p_{\pm 1}$ to be obtained in the maximization of entropy under constraints.

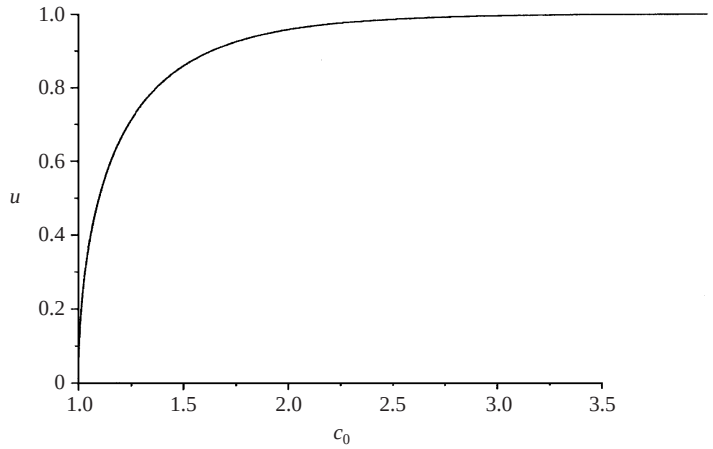

FIGURE 5. The parameter u versus the Lagrange parameter C_0, as the solution of (35).

Using (11), (23) we deduce that

$$\psi_{\pm 1} = R^2(B \pm u). \tag{32}$$

From (22) we can state that the two constant stream functions (32) have to be of opposite sign, so that $u > |B|$. Introducing (31) in the circulation constraint (23), and using (21), we obtain

$$A_{\pm 1} = \frac{1}{2}\left(1 \mp \frac{B}{u}\right). \tag{33}$$

Using these results, the energy (24) becomes

$$E \simeq E_A = \tfrac{1}{2}R^2(u^2 - B^2). \tag{34}$$

This relates the parameter u to the given energy E and asymmetry parameter B. Finally the condition that $f(p_{\pm 1})$ are maxima of f leads to

$$u = \tanh(C_0 u), \tag{35}$$

which determines the 'temperature' parameter C_0, as represented in figure 5. Therefore

all the quantities are determined from the asymmetry parameter B and from the parameter u, related to the energy by (34).

In the limit of low energy, $u \to |B|$, when for instance $B > 0$, then A_1 goes to zero, so that ψ_{-1} tends to occupy the whole domain. This state is the most mixed one compatible with the constraint of a given value of B (or equivalently a given initial patch area $A = (1 - B)/2$). In the opposite limit $u \to 1$, we see from (32) that in the two subdomains $q = \psi/R^2$ tends to the two initial PV levels $a_1 = 1 + B$ and $a_{-1} = -1 + B$. Thus, this state is unmixed. It achieves the maximum possible energy $E = \frac{1}{2}R^2(1 - B^2)$ under the constraint of a given patch area. We conclude that the parameter u, or the related 'temperature' C_0, characterizes the mixing of these two PV levels. We shall call u the segregation parameter, as it quantifies the segregation of the PV level a_1 (or its complement a_{-1}) between the two phases.

Let us now study the interface between the subdomains.

2.3.2. *Interior jets*

At the interface between two constant-stream-function subdomains, a strong gradient of ψ necessarily occurs, corresponding to a jet along the interface. To study these jets, we come back to the Gibbs state equation (18). We expect the Lagrange parameters α and C to be close to the zero-order parameters α_0 and C_0, computed in the previous subsection, so we use $\alpha = \alpha_0$ and $C = C_0$ to calculate the jet structure. In such a jet, we cannot neglect the Laplacian term in (18), but a boundary-layer-type approximation can be used: we neglect the tangential derivative with respect to the derivative along the coordinate normal to the interface, ζ. Accordingly, we neglect the inverse of the curvature radius of the jet with respect to $1/R$.

Thus, from the Gibbs state equation (18), using (30), we deduce the jet equation:

$$-\frac{\mathrm{d}^2\psi}{\mathrm{d}\zeta^2} + \frac{\psi}{R^2} = B - \tanh\left(C_0\left(B - \frac{\psi}{R^2}\right)\right). \tag{36}$$

As the stream function depends only on the normal coordinate ζ, the velocity is tangent to the interface, forming a jet with a typical width scaling with R. We thus make the change of variables defined by

$$\tau \equiv \frac{\zeta}{R}, \quad \phi \equiv -B + \frac{\psi}{R^2}, \tag{37}$$

leading to the rescaled jet equation

$$\frac{\mathrm{d}^2\phi}{\mathrm{d}\tau^2} = -\tanh(C_0\phi) + \phi. \tag{38}$$

The jet equation (38) is similar to a one-dimensional equation of motion for a particle (with the position ϕ depending on a time τ) under the action of a force $-\mathrm{d}U/\mathrm{d}\phi$ derived from the potential,

$$U(\phi) = \frac{\ln(\cosh(C_0\phi))}{C_0} - \frac{\phi^2}{2}, \tag{39}$$

represented in figure 3(b). In its trajectory the particle energy is conserved:

$$\frac{1}{2}\left(\frac{\mathrm{d}\phi}{\mathrm{d}\tau}\right)^2 + U(\phi) = \text{Const.} \tag{40}$$

Let $\phi_i \equiv \psi_i/R^2 - B$, $i = -1, 0, 1$, corresponding to the solutions ψ_i of the algebraic equation (20). From (32), we have $\phi_{\pm 1} = \pm u$. Note that the stationary limit of (38),

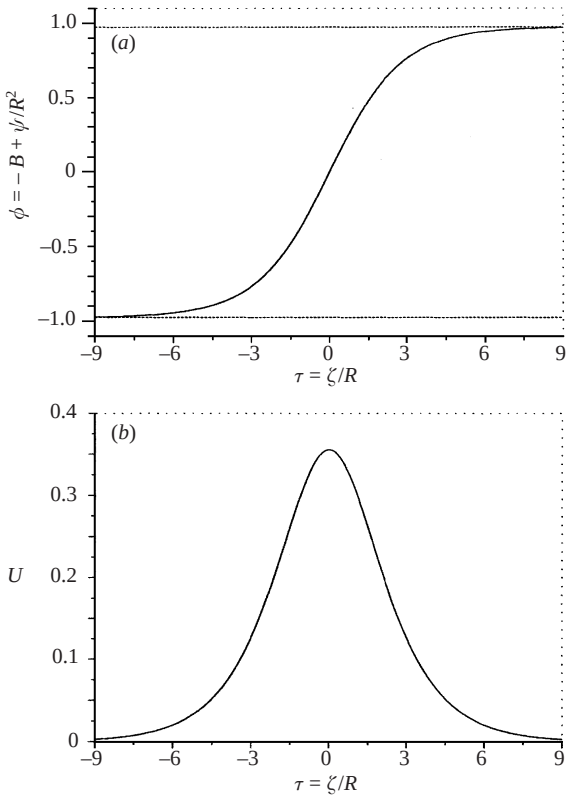

FIGURE 6. (a) Typical stream function profile in a jet ($u = 0.75$) versus the transverse coordinate $\tau = \zeta/R$, and (b) corresponding velocity profile.

which must be reached for $\lim_{\tau\to\pm\infty}$, yields (35) again. Moreover, the particle energy conservation (40) imposes the integrability condition,

$$U(\phi_{-1}) = U(\phi_1), \tag{41}$$

which is indeed satisfied due to the symmetry of the potential U. We note that the Lagrange parameter determination (30) and the symmetry of the probabilities (31) with respect to $\frac{1}{2}$ could have been deduced from this integrability condition (41) instead of minimizing the free energy (29) (we shall proceed in this way in § 3 to take into account the beta-effect).

The jet equation (38) has been numerically integrated. Figure 6 shows a typical stream function and velocity profile in the jets. Figure 7(a) shows that the jet width l is a decreasing function of the segregation parameter u, therefore a decreasing function of the total energy. Figure 7(b) shows the dependence on u of the total non-dimensional jet energy $e(u) = \frac{1}{2}\int_{-\infty}^{+\infty}(\mathrm{d}\phi/\mathrm{d}\tau)^2\,\mathrm{d}\tau$ and of the maximum non-dimensional jet velocity

$$v_{max}(u) = \sqrt{2\left(-\frac{u\log(1-u^2)}{\arg\tanh u} - \frac{u^2}{2}\right)}$$

(and two other quantities used in the next section).

As the jet structure (38) does not depend on the coordinate tangent to the jet, we can define the jet entropy (resp. energy, free energy) per unit length S_{Jet} (resp. E_{Jet},

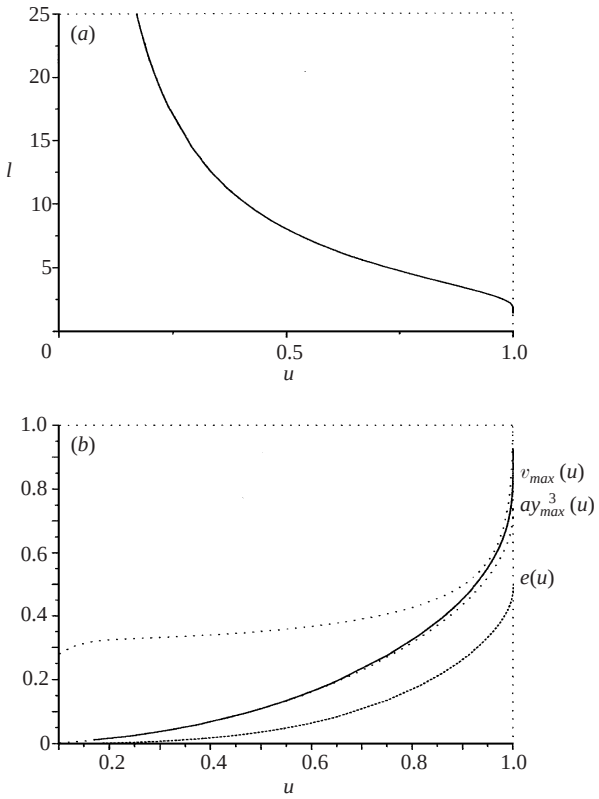

FIGURE 7. Jet properties versus the segregation parameter u. (a) Jet width l, defined as the width of the region with velocity greater than half the maximum jet velocity. (b) Maximum velocity v_{max}, jet kinetic energy $e(u)$ (dotted line), maximal extension of the vortices with topography: $ay^3_{max}(u)$ (81) and function $i(u)$ linking the segregation parameter u to the non-dimensional quantity $\sigma^* y^{*3}_{max}/(v^*_{max} l^{*2})$ (83) in the presence of topography.

F_{Jet}). Multiplied by the jet length, these quantities are the first-order corrections to the entropy (resp. energy, free energy). Using the change of variables (37), we calculate the jet entropy per unit length:

$$S_{Jet} = R \int_{-\infty}^{+\infty} [s(p(\tau)) - s(p_{\pm 1})]\, \mathrm{d}\tau,$$

where s is defined in (26), and $p_{\pm 1}$ are defined in (31). Using the probability equation (17) and (37) we obtain

$$S_{Jet} = R \int_{-\infty}^{+\infty} [\tilde{s}(\phi) - \tilde{s}(\phi_{\pm 1})]\, \mathrm{d}\tau \tag{42}$$

involving the function $\tilde{s}(\phi) \equiv \ln(\cosh(C_0\phi)) - C_0\phi \tanh(C_0\phi)$. Similarly we straightforwardly calculate the potential and kinetic energy per unit length for the jet

$$E^P_{Jet} = \frac{R^3}{2} \int_{-\infty}^{+\infty} (\phi^2 - \phi_1^2)\, \mathrm{d}\tau, \quad E^K_{Jet} = \frac{R^3}{2} \int_{-\infty}^{+\infty} \left(\frac{\mathrm{d}\phi}{\mathrm{d}\tau}\right)^2 \mathrm{d}\tau.$$

We use the integral (40) to calculate $\mathrm{d}\phi/\mathrm{d}\tau$ and conclude

$$E_{Jet} = R^3 \int_{-\infty}^{+\infty} [\tilde{g}(\phi) - \tilde{g}(\phi_{\pm 1})]\, \mathrm{d}\tau, \tag{43}$$

with $\tilde{g}(\phi) = -(\ln(\cosh(C_0\phi)))/C_0 + \phi^2$. Due to their symmetry, the jets provide no perturbation to the zero-order circulation, so there is no circulation term in the jet free-energy expression: $F_{Jet} = -S_{Jet} - C_0/R^2 E_{Jet}$. Then

$$F_{Jet} = C_0 R \int_{-\infty}^{+\infty} [\tilde{h}(\phi) - \tilde{h}(\phi_{\pm 1})]\, \mathrm{d}\tau \tag{44}$$

with $\tilde{h}(\phi) = -\phi(\phi - \tanh(C_0\phi))$.

Let us study the sign of F_{Jet}. As ϕ_1 satisfies $\phi_1 = \tanh(C_0\phi_1)$ and as $\phi(\tau)$ is an increasing function of τ with $\lim_{\tau\to+\infty} \phi(\tau) = \phi_1$ we conclude that $\tilde{h}(\phi) - \tilde{h}(\phi_1) > 0$ for any $\tau > 0$. Thus $F_{Jet} > 0$. Using the analogy with standard thermodynamics, the 'surface tension' is positive. This favours large 'bubbles' which minimize the interfacial length and therefore the corresponding free energy (44). Our initial hypothesis of well-separated domains with uniform ψ is thus supported, as discussed more precisely in the next subsection.

2.3.3. *Selection of the equilibrium structure*

The above analysis has permitted us to determine the areas of subdomains in which the stream function ψ takes the constant values $\psi_{\pm 1}$, but the subdomains shape is still to be selected. There is an analogy with two phases coexisting in thermodynamic equilibrium, for instance a gas bubble in a liquid medium, for which a classical thermodynamic argument explains the spherical shape of the bubble by minimizing its free energy, proportional to the bubble area. Our system is isolated rather than in a thermal bath, but the jet energy is small (of order R) with respect to the total energy. Therefore the subdomain interior behaves like a thermal bath with respect to the jet, so the usual argument on free-energy minimization applies. We shall now show this more precisely by directly maximizing the total entropy with constraints, taking into account the jet contribution.

A jet with length L has an entropy $S_{jet}L$ and energy $E_{jet}L$. Since the total energy $E = E_A(C) + LE_{Jet}$ is given, the jet has also an indirect influence on the area energy E_A. A small energy change δE_A results in a corresponding change in the area entropy $\delta S_A = -(C_0/R^2)\delta E_A$, from the condition (27) of zero first variations. Note that there is no area change δA since the jet is symmetric and therefore has no influence in the condition (12) of a given integral of p (the difference in p with respect to the case of two uniform patches with boundary at the jet centre has zero integral). Therefore, adding the direct and indirect contribution of the jet entropy leads to the total entropy

$$S = S_A(C_0) - F_{Jet}(C_0)L, \tag{45}$$

where $S_A(C_0)$ is the zero-order area entropy, obtained in the limit of vanishing jet width.†

We deduce from (45) that the maximization of the entropy is achieved by minimizing the total free energy $F_{Jet}L$, which we have proved to be positive at the end of the

† This reasoning to obtain the first-order entropy (45) can be made more rigorous by evaluating explicitly the first-order modification of the Lagrange parameter C (let, say, $C_1 \equiv C - C_0$) due to the jet energy, and the first-order modification of the Lagrange parameter α (let, say, $\alpha_1 \equiv \alpha - \alpha_0$) due to the jet curvature and computing the first-order entropy from its definition (15).

previous subsection. Thus we conclude that the maximum-entropy state minimizes the jet length, with the given area (33) of the subdomains.

The subdomain shape will therefore be a circle or a band. More precisely if $A_1 < 1/\pi$ the jet forms a circle enclosing the positive constant-stream-function domain (the jet bounds a cyclonic vortex), if $1/\pi < A_1 < 1-1/\pi$ two straight line jets form a band, and if $A_1 > 1 - 1/\pi$ the jet form a circle enclosing the negative constant-stream-function domain (the jet bounds an anti-cyclonic vortex).

The different types of solutions have been summarized in the (E, B) diagram of figure 2. The outer parabola is the maximum energy achievable for a fixed B: $E = R^2(1 - B^2)/2$. The interfaces between the straight jets and the circular jets correspond to $A_1 = 1/\pi$ or $A_{-1} = 1/\pi$. It has been calculated using (33) and (34): $E = R^2B^2(2\pi - 2)/(\pi - 2)^2$. Note that the maximum accessible energy is in R^2, but it has been scaled by the normalization condition (9) on PV levels, so the real energy is not bounded.

All this analysis assumes that the vortex size is much larger than the jet width l, given by figure 7. In other words, the area A_1 or A_{-1} (33) must be larger than $(2l)^2$. This is satisfied on the right of the dashed line in figure 2, representing the equality. The condition of a large vortex is clearly not satisfied on the low-energy (left) side of this line. The position of this dashed line depends on the numerical value of R (it has been numerically computed here for $R = 0.03$), and it moves closer to the origin as $R \to 0$. We shall now determine the statistical equilibrium in this case of low energy.

In the limit of small energy with fixed B and (small) fixed R, axisymmetric vortices are obtained (see Appendix A). In the limit of small E and B, i.e. the neighbourhood of the origin in the phase diagram of figure 2, the jet tends to develop on the scale of the whole domain, so the approximation of a localized jet, or an isolated axisymmetric vortex, fails. Indeed from (34), $u \to |B| \ll 1$. Figure 7 shows that for $|u| \ll 1$, the jet width diverges.

In this limit of small E and B, we can linearize the Gibbs states equation (18). The solutions are then expressed in terms of the eigenmodes of the Laplacian. The work of Chavanis & Sommeria (1996) for Euler's equation directly applies here: the results are unchanged by the linear deformation term ψ/R^2.

Only the first eigenmodes of the Laplacian can be entropy maxima. With the periodic boundary conditions, a sine function of one of the coordinates, for instance y, is thus selected. This corresponds to the low-energy limit of the two jet configuration shown in figure 2. The next eigenmode, in $\sin(\pi x)\sin(\pi y)$, has the topology of the vortex states. A competition between these two modes is expected in the neighbourhood of the origin for small E and B. Note that the validity of the linear approximation is limited to a smaller range of parameters than in the Euler case, and this range of validity becomes smaller and smaller as $R \to 0$. The dominant solution with uniform subdomains and interfacial jets relies by contrast on the tanh-like relation between the PV and stream function, and it is genuinely nonlinear.

3. The influence of beta-effect and bottom topography

We now introduce a beta-effect, or a mean sublayer zonal flow (topography), with the term $h(y)$ in (1). The two cases of a linear $h(y)$ (beta-effect and/or uniform velocity for the sublayer flow) and a quadratic $h(y)$ will be considered. For that study, we first need to adapt the previous results to the channel geometry, which represents a zonal band around a given latitude.

3.1. *The dynamical system*

Let us consider the barotropic QG equations (1), (2) and (3) in a channel $D = [-\frac{1}{2}, \frac{1}{2}]^2$ with the velocity $\boldsymbol{v}$ tangent to the boundary for $y = \pm\frac{1}{2}$ and 1-periodicity in the zonal direction. Due to the impermeability condition, the stream function must be x independent at each boundary. The difference between the two boundary values is equal to the physical x-wise momentum (the integral of velocity), a conserved quantity. We can always set this momentum to zero by a change of reference frame, with a zonal velocity V moving with the centre of mass of the fluid layer, and a corresponding change of the deep flow, resulting in an additional beta-effect $h \to h + (Vy/R^2)$. We therefore choose for the boundary conditions a constant ψ, denoted ψ_b, which is the same on the two boundaries $y = \pm\frac{1}{2}$.

As in § 2, we need to specify the gauge constant in the stream function ψ, and we generalize the integral condition (4) as

$$\frac{\langle\psi\rangle}{R^2} - \langle h(y)\rangle = 0. \tag{46}$$

The total mass $\langle\psi\rangle$ is then constant in time (but not the boundary value ψ_b in general). With these conditions, the Dirichlet problem (2) has a unique solution ψ for a given PV field q.

The integral of any functions of the potential vorticity (8) is still conserved. Let in particular Γ be the global PV, or circulation:

$$\Gamma \equiv \langle q\rangle = \int_D -\Delta\psi \, \mathrm{d}^2\boldsymbol{r} = \int_{\partial D} \boldsymbol{v}\cdot \mathrm{d}\boldsymbol{l}. \tag{47}$$

In contrast to the doubly periodic boundary conditions, the circulation Γ is not necessarily equal to zero. The expression for the energy in terms of the PV (see equation (7)) is therefore modified (due to the boundary term in the integration by parts):

$$E = \frac{1}{2}\int_D \left[(\nabla\psi)^2 + \frac{\psi^2}{R^2}\right] \mathrm{d}^2\boldsymbol{r} = \frac{1}{2}\int_D (q + h(y))\psi \, \mathrm{d}^2\boldsymbol{r} - \tfrac{1}{2}\Gamma\psi_b. \tag{48}$$

Due to the invariance under zonal translation of the system, another conserved quantity exists:

$$M = \int_D yq \, \mathrm{d}^2\boldsymbol{r}. \tag{49}$$

This constant moment fixes the 'centre of mass' latitude for the PV field.

3.2. *General form of the Gibbs states in the channel geometry*

Let us consider the statistical mechanics for a two-PV-level configuration: the initial state is made up of patches with two levels of potential vorticity, $q = a_1$ and $q = a_{-1}$, occupying respectively the areas A and $(1 - A)$ in D. We keep the normalization (9) and definition (10) for B. Now, since the circulation Γ is non-zero, the area A is related to B by $A = (1-B)/2 + \Gamma/2$. The boundary condition ψ_b leads to a boundary term in the integration by parts of the energy variation (16). Let γ be the Lagrange multiplier associated with the conservation of the momentum M.

Adapting the periodic case computations, we then calculate the probability equation

and the Gibbs state equation:

$$p = \frac{1 - \tanh(\alpha' - (C\psi/R^2) + \gamma y)}{2}, \tag{50}$$

$$q = -\Delta\psi + \frac{\psi}{R^2} - h(y) = B - \tanh\left(\alpha' - \frac{C\psi}{R^2} + \gamma y\right), \tag{51}$$

with $\alpha' \equiv \alpha + C\psi_b/R^2$. We have considered ψ_b as a constant parameter in the maximization process: it is eventually imposed by the condition (46) on the resulting equilibrium flow. These results generalize (17) and (18) of § 2.

In the case of a Gibbs state depending on x, the Lagrange parameter γ is related to a zonal propagation of the equilibrium structure. The statistical theory only predicts a set of equilibria shifted in x, but introducing the result back in the dynamical equation yields the propagation. Indeed the Gibbs state equation (51) is of the form $q = f(\psi, y)$, which can be inverted (as it is monotonic in ψ, see Robert & Sommeria (1991)) to yield

$$\psi = g(q) + R^2\frac{\gamma y}{C}, \tag{52}$$

where g is a function of the potential vorticity. From this relation we calculate the velocity using (3): $\boldsymbol{v} = R^2(\gamma/C)\boldsymbol{e}_x - g'(q)\boldsymbol{e}_z \wedge \nabla q$. As PV is advected (equation (1)) we obtain

$$\frac{\partial q}{\partial t} + R^2\frac{\gamma}{C}\frac{\partial q}{\partial x} = 0. \tag{53}$$

Thus the PV field is invariant in a frame propagating with the zonal speed $V_{sr} = R^2(\gamma/C)$.

3.3. *The limit of small Rossby deformation radius*

In this subsection we analyse the Gibbs state equation (51) in the limit of small deformation radius ($R \ll 1$). The main difference with the periodic case resides in the latitudinally dependent topography $h(y)$, resulting in two effects. First the subdomains of uniform PV are no longer strictly uniform, and they contain a weak zonal flow. Secondly the jet curvature is no longer constant in general, but depends on the local topography. As in the periodic case, the Laplacian term in the Gibbs state equation (51) will be neglected, except possibly in an interior jet and in the vicinity of the boundaries $y = \pm\frac{1}{2}$ (boundary jets).

Outside such jets, (51) reduces to the algebraic equation

$$\frac{\psi}{R^2} - h(y) = B - \tanh\left(\alpha' - C\frac{\psi}{R^2} + \gamma y\right). \tag{54}$$

This is like (20), but replacing the constants B by $B + h(y)$ and α by $\alpha' + \gamma y$. The three solutions can be still visualized using figure 3, but the position of the straight line with respect to the tanh curve now depends on y, due to the terms $h(y)$ and γy. We assume that this dependence is linear in y or varies on scales much larger than R so that the Laplacian term remains indeed negligible. The zero-order Lagrange parameters α', C, γ, involved in this expression, can be obtained by directly maximizing the entropy by the same method as in § 2.3.1. A relation between the jet curvature and topography is then obtained at first order. This approach is developed in Appendix B.

However it is more simple to proceed differently: we start from the jet equation and show that its integrability condition (41) is modified, providing a relation between the jet curvature and topography. To capture this effect, we take into account the radius

of curvature of the jet, denoted r, assumed constant across the thin jet. From the Gibbs state equation (51), using the boundary layer approximation, we thus obtain the jet equation in terms of the transverse coordinate ζ (then by definition ψ does not depend on the along-jet coordinate):

$$-\frac{\mathrm{d}^2\psi}{\mathrm{d}\zeta^2} - \epsilon\frac{1}{r}\frac{\mathrm{d}\psi}{\mathrm{d}\zeta} + \frac{\psi}{R^2} - h(y) = B - \tanh\left(\alpha' - C\frac{\psi}{R^2} + \gamma y\right). \tag{55}$$

We have introduced $\epsilon = \pm 1$ to account for the direction of curvature (keeping $r > 0$). We define $\epsilon = 1$ (resp. -1) if the curvature of the jet is such that ψ_1 (resp. ψ_{-1}) is in the inner part of the jet. Note that, in the case of a vortex, as in our notation ψ is proportional to the pressure in the southern hemisphere, the case $\epsilon = 1$ (resp. $\epsilon = -1$) corresponds to an anticyclone (resp. a cyclone) (the sign is reversed in the northern hemisphere).

Let us make the change of variables

$$\tau \equiv \frac{\zeta}{R}, \quad \phi \equiv -\frac{\alpha' + \gamma y}{C} + \frac{\psi}{R^2}. \tag{56}$$

We assume that the variations of y within the jet width are negligible ($R \ll$ scale of variation of $h(y)$), so that y is treated as a constant. Then we obtain the jet equation:

$$-\frac{\mathrm{d}^2\phi}{\mathrm{d}\tau^2} - \epsilon\frac{R}{r}\frac{\mathrm{d}\phi}{\mathrm{d}\tau} + \phi + \frac{\alpha' + \gamma y}{C} = B + h(y) + \tanh(C\phi), \tag{57}$$

with $\phi \to \phi_{\pm 1}$ for $\tau \to \pm\infty$, where again $\phi_{\pm 1}$ corresponds to the solutions of the algebraic equation (54), rescaled as

$$\phi + \frac{\alpha'}{C} - B + \frac{\gamma y}{C} - h(y) = \tanh(C\phi). \tag{58}$$

Let us consider, as in § 2.3.2, the analogy of equation (57) with the equation of motion of a particle in the potential:

$$U(\phi) = \frac{\ln\cosh(C\phi)}{C} - \frac{\phi^2}{2} + \left(B + h(y) - \frac{\alpha' + \gamma y}{C}\right)\phi. \tag{59}$$

Integration of (57) from $-\infty$ to $+\infty$ imposes the integrability condition:

$$U(\phi_1) - U(\phi_{-1}) = \epsilon\frac{R}{r}\int_{-\infty}^{+\infty}\left(\frac{\mathrm{d}\phi}{\mathrm{d}\tau}\right)^2 \mathrm{d}\tau. \tag{60}$$

The second term of the left-hand side of equation (57) can be interpreted formally as a friction term: if $\epsilon = 1$, the 'particle' starting from rest at ϕ_1 can reach a state of rest at ϕ_{-1} only if the difference of 'potential' corresponds to the energy loss (60) by friction (if $\epsilon = -1$ the same is true in the reverse direction).

With our thin jet assumption $R \ll r$, this friction term (right-hand side of (60)) is a correction of order R/r: $U(\phi_1) - U(\phi_{-1}) = O(R/r)$. We first neglect it to obtain the zero-order results, so we write $U(\phi) = U(\phi_{-1})$ and the two hatched areas in figure 3 must be equal. Due to the symmetry of the tanh-function, this clearly implies that the central solution of the rescaled algebraic equation (58) must be $\phi_0 = 0$, so that $\alpha_0'/C_0 - B + \gamma y/C_0 - h(y) = 0$ (denoting the zero-order Lagrange parameters by the index 0). This is possible at different latitudes y only if $\gamma y/C_0 - h(y) = 0$, or is of order R (so that it can be neglected at zero order). Then the integrability condition becomes

$$\alpha_0' = C_0 B. \tag{61}$$

Furthermore $\phi_{\pm 1}$ are symmetric with respect to 0, of the form $\phi_{\pm 1} = \pm u$, determined by equation (35), like in § 2.3. This parameter u is again related to the energy by (34). Finally, the terms $\gamma y/C_0 - h(y) = 0$ and the curvature term disappear in the jet equation (57), which therefore reduces to (38), discussed in § 2.3.2.

The first-order solution outside the jet is obtained as a small correction $\delta\phi_{\pm 1}$ to the zero-order solutions $\pm u$, with also a small correction α_1 and C_1 to the parameters α_0'/C_0 and C_0:

$$\phi_{\pm 1} = \pm u + \delta\phi_{\pm 1}(y), \quad \frac{\alpha'}{C} = \frac{\alpha_0'}{C_0} + \alpha_1, \quad C = C_0 + C_1. \tag{62}$$

From (60), we deduce that $U(\phi_1) - U(\phi_{-1})$ has the sign of ϵ. As may be seen in figure 3, when α_1 is positive, the line $\phi + (\alpha'/C)$ moves upward, so that $U(\phi_1) < U(\phi_{-1})$. Thus α_1 has sign opposite to the sign of $U(\phi_1) - U(\phi_{-1})$; and we conclude that $-\epsilon\alpha_1$ is always positive. Introducing this expansion (62) in the algebraic equation (58), using the zero-order results (35) and (61), we obtain

$$\delta\phi_{\pm 1}(y) = \frac{-\alpha_1 C_0 \pm C_1 u(1-u^2) - (\gamma/C_0)y + C_0 h(y)}{1 - C_0(1-u^2)}. \tag{63}$$

The integrability condition (60) now provides the curvature of the jet. We can approximate the right-hand side of this relation, of order R, by the zero-order jet profile solution of (38), denoting

$$e(u) \equiv \frac{1}{2}\int_{-\infty}^{+\infty} \left(\frac{\mathrm{d}\phi}{\mathrm{d}\tau}\right)^2 \mathrm{d}\tau \tag{64}$$

(this function is represented in figure 7(*b*)). The left-hand side of (60) can be expanded using (62), (63). We first expand the expression (59) of the potential,

$$U(\phi) = U_0(\phi) + C_1/C_0[\phi \tanh(C_0\phi) - \log\cosh(C_0\phi)/C_0] + [h(y) - \gamma y/C_0 - \alpha_1]\phi.$$

We can approximate $\phi \simeq \pm u$ in the correction terms, and expand $U_0(\phi) = U_0(\pm u) + \mathrm{d}U_0/\mathrm{d}\phi(\pm u)$. The zero-order equilibrium condition requires that $\mathrm{d}U_0/\mathrm{d}\phi(\pm u) = 0$, so that (60) becomes

$$\epsilon u\left(h(y) - \frac{\gamma y}{C_0} - \alpha_1\right) = e(u)\frac{R}{r}. \tag{65}$$

This equation (65) expresses the dependence in latitude y of the curvature radius r of the curve on which the jet is centred (the curve where ϕ is equal to zero), thus defining the shape of the subdomain interface as a function of the topography.

Without topography and for $\gamma = 0$, we obtain a constant jet curvature. The same result was obtained in § 2.3.3 by a different argument of free-energy minimization. The parameter u, related to the energy by (34) and to C_0 by (35), quantifies the strength of the jet. By contrast, the vortex area is determined by the constraint on PV patch area (parameter B), but it is also related to the jet curvature, proportional by (65) to the small shift α_1 in chemical potential and temperature. Likewise the equilibrium temperature at a liquid–gas interface depends slightly on the bubble curvature, due to capillary effects.

As explained at the end of § 3.2 the parameter γ is linked to the zonal propagation speed of the structure. The term γy in (65), combined with a usual beta-effect (linear topography term $h(y)$), leads to an oscillation with latitude y of the jet curvature $1/r$, i.e. a meandering jet. Another possibility is an exact compensation of the beta-effect by the γy term, leading to a propagating circular vortex, and the selection between

these two alternatives is discussed in the next subsection. An oval-shaped, zonally elongated vortex, such as on Jupiter, is obtained when this compensation occurs, but with an additional quadratic topography $h(y)$. Indeed, to obtain a zonally elongated vortex, supposed to be latitudinally centred on zero, the radius of curvature of the jet must decrease for $y > 0$ and increase for $y < 0$. As a consequence, we deduce from (65) that the topography must be extremal at the latitude on which the vortex is centred: recalling the sign discussion of ϵ at the beginning of this section, one can verify that $h(y)$ actually admits a minimum in the cyclonic case and a maximum in the anticyclonic case.

Our expansion also provides the velocity $\boldsymbol{v}$ outside the jets, by differentiating (63) with respect to y. Coming back to the stream function ψ, using (56),

$$\boldsymbol{v} = R^2 \left(\frac{\mathrm{d}h/\mathrm{d}y - \gamma(1-u^2)}{1 - C_0(1-u^2)} \right) \boldsymbol{e}_x, \tag{66}$$

where $\boldsymbol{e}_x$ is the eastward unit vector. The velocity is therefore a constant plus a term proportional to the local beta-effect $\mathrm{d}h/\mathrm{d}y$. Notice that the corresponding shear $\mathrm{d}\boldsymbol{v}/\mathrm{d}y$ is stronger than the deep shear $\mathrm{d}^2\psi_d/\mathrm{d}y^2 = R^2\mathrm{d}^2h/\mathrm{d}y^2$ by the factor $[1 - C_0(1-u^2)]^{-1} > 1$. This zonal velocity can be related to the jet curvature, eliminating the topography between (66) and (65),

$$\boldsymbol{v} = R^2 \left(\frac{\gamma}{C_0} + \frac{\epsilon e(u)}{u(1 - C_0(1-u^2))} \frac{\mathrm{d}}{\mathrm{d}y} \left(\frac{R}{r} \right) \right) \boldsymbol{e}_x. \tag{67}$$

We deduce from this last equation that the zonal velocity is equal to $R^2\gamma/C_0$ at the latitude of extremal curvature, on which the elongated vortex is centred. This is just the speed of translation V_{sr} of the structure, so that the vortex does not propagate with respect to its surroundings. We also deduce that the shear is cyclonic when the longitudinally elongated vortex is a cyclone and anticyclonic when it is an anticyclone (see the previous discussion on the sign of ϵ and the extrema of h).

The above derivation of the jet shape via the link (65) between the latitudinally dependent topography and the radius of curvature of the jet may not determine uniquely the jet shape. Several solutions of (65) with several values of the first-order Lagrange parameter α_1 but corresponding to the same energy and initial PV patch areas may exist. A solution with two straight zonal jets flowing respectively westward and eastward, and enclosing a band of slowly varying PV may be, for instance, in competition with an oval shaped jet satisfying (65). The choice between such solutions will be made by entropy maximization. We thus generalize the first-order entropy (45) of § 2.3.3:

$$S = S_A(C_0) - F_{Jet}(C_0)L + 2\epsilon C_0 u \int_{A_\epsilon} [h(y) - \gamma y/C_0 - \alpha_1] \, \mathrm{d}^2\boldsymbol{r}, \tag{68}$$

where $F_{Jet}(C_0)$ is the jet free energy (44) per unit of length. As we seek entropy maxima, this shows that anticyclonic (resp. cyclonic) vortices will preferably be near maxima (resp. minima) of the topography $(h(y) - \gamma y/C_0)$. We understand furthermore the vortex oval shape (65) to be the result of the competition between a trend to minimize the jet length, due to the second term in the right-hand side of (68) and a trend for PV to lay close to topography extrema (we prove in Appendix B that maximization of the entropy (68) does lead to the jet shape equation (65)). With respect to oval-shaped vortices, two alternating straight jets enclosing an extremum of the topography will be favoured because they allow a better distribution of PV

near this topography extremum, but not favoured because they will require a greater jet length. This competition will be analysed in detail in the case of a quadratic topography in § 3.5.

Let us summarize our approximations. Writing the jet equation (55), when making the boundary layer approximation, we have assumed $R \ll r$. We also assumed that in the jet within the topography can be considered as a constant. If $1/\sqrt{a}$ is a typical length scale for the topography variation, this gives $aR^2 \ll 1$. Moreover we have assumed that the topography effect $h(y) - \gamma y/C_0$ remains small along the jet. If L_V denotes the jet extent (for example a vortex latitudinal size) this approximation is valid as long as $aL_V^2 \ll 1$.

3.4. *Influence of a linear beta-effect on the statistical equilibrium jets*

Let $h(y) \equiv -\beta y$ in this section. β may mimic the beta-effect or a uniform velocity in the sublayer (but we will refer it as the beta-effect).

A first class of equilibrium states corresponds to a single solution $\psi(y)$ of the algebraic equation (54). This determines a smooth zonal flow, possibly with intense jets at the boundaries $y = \pm\frac{1}{2}$. The solution depends on the unknown parameters C, α' and γ, which are indirectly determined by the energy E, momentum M, and the condition $\langle\psi\rangle = 0$. The limit of small energy corresponds to $C \to \infty$, for which we can neglect the term ψ/R^2 on the left-hand side of (54), which then reduces to $\psi = (R^2/C)[\arg\tanh(\beta y - B) + \gamma y + \alpha']$. This corresponds to arbitrarily small values of ψ (small energy) as $C \to \infty$.

When the particular energy value $E = R^2\beta^2/24$ is reached, a uniform PV is possible, with $\psi/R^2 = -\beta y$. Then PV mixing is complete, which clearly maximizes the mixing entropy. In this case,$\gamma = -C\beta$, so that γy cancels the term $C\psi/R^2$ in (54). Physically, the uniform westward zonal velocity,

$$v_m = -R^2\beta, \tag{69}$$

tilts the free-surface with uniform slope through the geostrophic balance, and the corresponding topographic beta-effect exactly balances the imposed beta-effect.

For a still higher energy, a first possibility is that again

$$\gamma = -C\beta \tag{70}$$

so that the beta-effect is exactly balanced by the γy term in the jet equation of the previous subsection. This cancellation is directly obtained in the general Gibbs state equations (50) and (51). Indeed, the modified stream function $\psi' = \psi + R^2\beta y$ satisfies the same equations as in the doubly-periodic case. Therefore in the limit of small R, the Gibbs states are made up of subdomains with uniform ψ' (uniform PV), separated by straight zonal jets or circular vortices. Such vortices move westward at the same velocity v_m, according to (53), so they are simply entrained by the background flow, without relative propagation (this can be physically understood by the cancellation of the beta-effect).

The selection of the subdomain areas and PV values is as in the periodic case of § 2, just replacing ψ by $\psi' = \psi - \beta R^2 y$. Therefore we obtain again probabilities $p_{\pm 1} = (1 \pm u)$ in the two subdomains with respective areas $A_{\pm 1}$ given by (33), and stream function

$$\psi_{\pm 1} = R^2(B \pm u) - R^2\beta y. \tag{71}$$

From this relation, we can calculate the energy $E = \frac{1}{2}(\psi_{-1}^2 A_{-1} + \psi_1^2 A_1)/R^2$, so the

energy condition (34) then becomes

$$E = \frac{R^2}{2}(u^2 - B^2) + \frac{R^2\beta^2}{24}. \tag{72}$$

Therefore these solutions with cancelled beta-effect can be obtained only beyond a minimum energy $R^2\beta^2/24$, corresponding to the potential energy of the surface tilting associated with the drift velocity v_m. Then the excess energy will control the organization in two uniform PV areas.

The shape of these subdomains can again be obtained by minimization of the jet free energy. However, unlike in the periodic case, jets occur at the boundaries $y = \pm\frac{1}{2}$ as well as at subdomain interfaces. Indeed, such boundary jets are in general necessary to satisfy $\langle \boldsymbol{v} \rangle = 0$, or equivalently that the stream function ψ_b must be equal at the two boundaries $y = \pm\frac{1}{2}$. In particular, the solutions (71) necessarily involve a stream function difference (or mass flux) $-R^2\beta$ associated with the drift velocity v_m. This stream function difference must be compensated by boundary eastward jets with opposite total mass flux. By analysing the competition between boundary and interior jets, we can show that for two PV levels with similar initial areas a single eastward jet, separating two regions of uniform PV and weak westward drift, is the selected state (instead of the two opposite jets in the periodic case). In the case of a strong PV level with a small initial area, the system is organized into a circular vortex as in the periodic case. In the limit $u \to |B|$, as one of the areas $A_{\pm 1}$ goes to zero, the jet approximation fails. The corresponding analysis of axisymmetric vortices and of the linear approximation for the Gibbs states, as performed in § 2, is still valid here.

Up to now we have ignored the constraint of the momentum M expressed by (49). This constraint imposes the latitude y_0 of the equilibrium structure (a circular patch or a zonal band with uniform PV). For instance in the case $B > 0$, for which $A_1 > A_{-1}$ (as seen from (33)), we define $y_0 \equiv \int_{A_1} y \, \mathrm{d}^2\boldsymbol{r}/A_1$. Then

$$M \equiv \int_D yq \, \mathrm{d}^2\boldsymbol{r} = \int_{A_1} y(B+u) \, \mathrm{d}^2\boldsymbol{r} + \int_{A_{-1}} y(B-u) \, \mathrm{d}^2\boldsymbol{r} = 2uy_0A_1. \tag{73}$$

We thus deduce the latitudinal position of the equilibrium structure:

$$y_0 = \frac{M}{2uA_1}. \tag{74}$$

In the case of a single eastward jet, the subdomain position has already been fixed by the area ($y_0 = A_1/2$). Then the only possibility for satisfying a moment M different from uA_1^2 is that the jet oscillates in latitude with some amplitude λ_0 (then $M - uA_1^2 \simeq u\lambda_0^2$). This is possible if $\gamma \neq -\beta C$ according to (65), which becomes

$$\frac{1}{r} = b(y - y_0), \tag{75}$$

where $b \equiv -(u(\gamma + \beta C))/(2Ce(u)R) < 0$ and $y_0 \equiv \alpha_1/b$. This equation clearly leads to a jet oscillating around the mean latitude y_0 (as the curvature r is positive for $y < y_0$ and negative for $y > y_0$; recall that the curvature is by definition positive when positive PV is in the inner part of the jet). Note that this oscillation propagates eastward at speed $R^2\gamma/C$ (given by (53)). Since $b < 0$, $\gamma/C > -\beta$, this speed is eastward with respect to the background drift v_m (69). We shall not give a complete analysis of this situation here, which could be relevant for the Earth's atmosphere.

3.5. *Influence of quadratic topography on the statistical equilibrium jets*

As explained in § 3.3, in the limit of small Rossby deformation radius R, the Gibbs state equation has solutions consisting of a vortex bounded by a strong jet on the scale of R. This corresponds to the case of an initial patch with strong PV and small area (the asymmetry parameter B is sufficiently large) with an energy sufficiently strong to give a structure of closed jet (see figure 10 below). In the presence of moderate topography $h(y)$, this internal jet is no longer circular but its radius of curvature $r \ll R$ depends on y according to (65). We have seen in the previous subsection that linear topography $h(y) = -\beta y$ leads to oscillating jets, or to circular jets when $\gamma = -C\beta$. We shall discuss here how a quadratic term in $h(y)$ modifies the shape of the closed jets. We therefore assume topography $h(y)$ of the form

$$h(y) \equiv -aRy^2 + by. \tag{76}$$

This corresponds to a uniform deep zonal shear, with velocity $v_d = R^2 \mathrm{d}(h-\beta y)/\mathrm{d}y = R^2(-2aRy + b - \beta)$. We have introduced the non-dimensional parameter R to stress the intervention of the topography at first order in our development. We focus our attention on vortex solutions, seeking closed curve solutions of equation (65). The vortices will be typically oval shaped like the ones seen on Jupiter. We then study how this shape (for instance the ratio of the larger axis of the oval to the smaller one) depends on the topography (sublayer flow) and on the jet parameters. Application of these results to Great Red Spot observations will be discussed in next section.

To make equation (65) more explicit, let s be a curvilinear parameterization of our curve, $\boldsymbol{T}(s)$ the tangent unit vector to the curve and $\theta(s)$ the angular function of the curve defined by $\boldsymbol{T}(s) = (\cos\theta(s), \sin\theta(s))$ for any s. Then the radius of curvature r of the curve is linked to $\theta(s)$ by $1/r = \mathrm{d}\theta/\mathrm{d}s$ and (65) yields the differential equations

$$\frac{\mathrm{d}\theta}{\mathrm{d}S} = -dY^2 + 1, \tag{77}$$

$$\frac{\mathrm{d}Y}{\mathrm{d}S} = \sin\theta(S), \tag{78}$$

$$\frac{\mathrm{d}X}{\mathrm{d}S} = \cos\theta(S). \tag{79}$$

In the above set of equations the space coordinates X, Y and S have been rescaled with the length $c' \equiv (e(u)/u)(-\varepsilon\alpha_1 + (b-\gamma/C_0)^2/4\varepsilon a)^{-1}$, such that $c'X = x$, $c'Y = y - y_0$, $c'S = s$, and $d = (\epsilon a u c'^3)/e(u)$, $y_0 = (\gamma/C_0 - b)/2aR$. Note that as explained in § 3.3, $\epsilon\alpha_1 < 0$. We further assume that $\varepsilon a > 0$ in accordance with the analysis of § 3.3, showing that the topography admits a maximum when $\varepsilon > 0$ (anticyclone) and a minimum when $\varepsilon > 0$ (cyclone). Thus $c' > 0$ and $d > 0$.

We first note that the two variables θ and Y are independent of X. We will therefore consider the system formed by the first two differential equations (77), (78). It is easily verified that this system is Hamiltonian, with θ and Y the two conjugate variables and

$$H \equiv \cos\theta - d\frac{Y^3}{3} + Y \tag{80}$$

the Hamiltonian. Thus H is constant on the solution curves. We look for vortex solutions of our problem (77), (79) and (78) so we require θ to be a monotonic function of S. Moreover the curves must close, that is X and Y must be periodic. For symmetry reasons, it is easily verified that the solutions of (77), (79) and (78) with

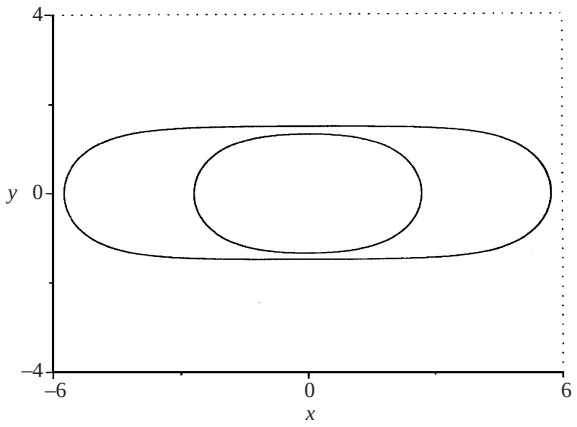

FIGURE 8. Typical subdomain shape with topography $h(y) = ay^2$. For the inner curve, the parameter d has been chosen such that the ratio of the length to the width is 2 as on Jupiter's GRS. For the outer curve, the parameter d is very close to its maximum value $d = \frac{4}{9}$. The shape is then very elongated, with quasi-parallel latitudinal boundaries, as for instance the Jovian cyclonic vortices ('Barges') described by Hatzes *et al.* (1981). The total velocity field is an intense jet of width l along this curve superposed onto the background zonal shear flow (67).

initial conditions $\theta(0) = \frac{1}{2}\pi$, $Y(0) = 0$ ($H = 0$) and some $X(0)$ are periodic. We prove in Appendix C that these initial conditions are the only ones leading to closed curves. The resulting vortex is then symmetric with respect to the latitude y_0. In the reference frame of the vortex, γ is equal to zero (see (53)); thus y_0 is the actual maximum of the topography. This shows that vortex solutions of the jet shape equation (65) are localized on extrema of the topography, in accordance with maximization of the first-order entropy (68). We also prove in Appendix C that the solutions of (77), (79) and (78) when $d > d_{max} \equiv \frac{4}{9}$ do not define θ as a monotonic function of S. They contain double points and thus are not possible solutions for our problem. Given these initial conditions, we can easily prove that the structure has both a zonal and a latitudinal symmetry axis passing through y_0.

To study the shape of the jets, we numerically solve equations (77), (79) and (78) with initial conditions: $\theta(0) = \frac{1}{2}\pi$, $y(0) = 0$. We obtain closed curves with oval shapes, as shown in figure 8. In figure 9 we show the half-width, the length and the aspect ratio of these vortices versus the parameter d. When d tends to $\frac{4}{9}$, the vortex width tends to a maximum value, $Y_{max} = \frac{3}{2}$, whereas the length diverges, so that the vortices are very elongated. We can see in figure 9 that this maximum width Y_{max} is nearly reached, and $d \simeq \frac{4}{9}$, for an aspect ratio of 2, corresponding of the Great Red Spot. From this value of d we can then compute the scaling parameter c'. This permits us to deduce that the actual vortex half-width y_{max} depends only on a and on the segregation parameter u:

$$y_{max} = \left(\frac{3e(u)}{2\epsilon a u}\right)^{1/3} \tag{81}$$

(for elongated vortices).

In summary, we have deduced all the jet properties as functions of the physical parameters (deformation radius R, topography a, and asymmetry parameter B representing the initial vortex patch areas) and of the segregation parameter u, related to an *a priori* unknown 'temperature'. The latitudinal half-width y_{max} of the vortex (annular jet), the jet width $Rl(u)$ and its maximum velocity $Rv(u)$ are represented in

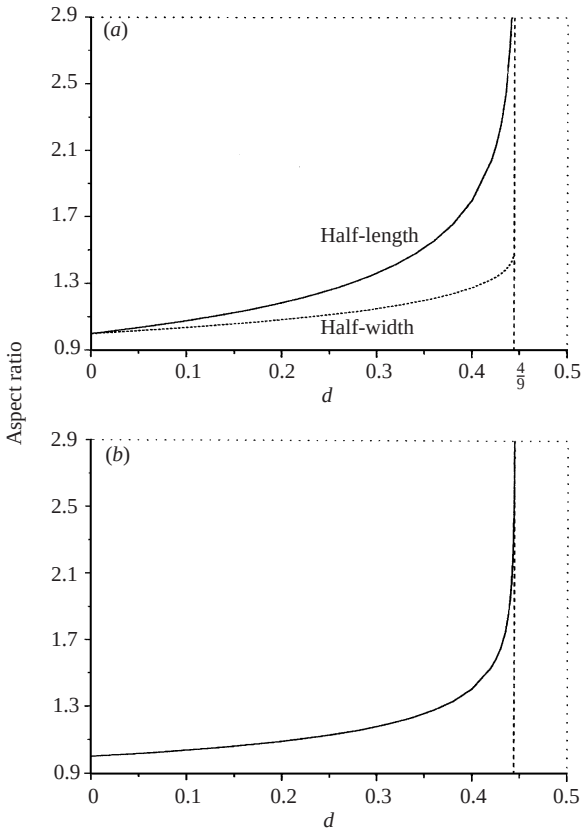

FIGURE 9. (*a*) Subdomain non-dimensional length and width versus the parameter d (topography $h(y) = ay^2$). (*b*) Subdomain aspect ratio versus the parameter d.

figure 7. Once the vortex width is obtained, the length (in longitude), or equivalently the vortex area A_1, is given from the parameter B by (33). We have also obtained the zonal velocity (66) outside the vortex, which yields a zonal shear (using the topography specification (76)) of $2aR^3\sigma(u)$ with $\sigma(u) = (1 - ((\arg\tanh u)/u)(1-u^2))^{-1}$ (a decreasing function of u, taking values from ∞ to 1 for u in the interval]0,1[).

To make connections with observations on Jupiter, we must come back to the dimensional variables, denoted by a star supersript. We need, in particular, to change the time unit, by introducing the difference in the two physical PV levels $a_1^* - a_{-1}^*$ (instead of the normalization (9)). The four previous relations now read

$$\left.\begin{aligned} y_{max}^{*3} &= \frac{3e(u)(a_1^* - a_{-1}^*)}{4ua^*}, \quad \sigma^* = 2a^*R^{*3}\sigma(u), \\ v_{max}^* &= \frac{(a_1^* - a_{-1}^*)R^*v(u)}{2}, \quad l^* = R^*l(u). \end{aligned}\right\} \tag{82}$$

These four relations (valid for elongated vortices) clearly relate the four free parameters of our model u, R^*, a^* and $(a_1^* - a_{-1}^*)$ to four easily measured vortex characteristics: the latitudinal extent of the vortex y_{max}, the shear around the vortex σ^*, the maximum jet velocity v_{max}^*, and the jet width l^*. These four relations may be easily inverted. In particular the segregation parameter u is determined by the

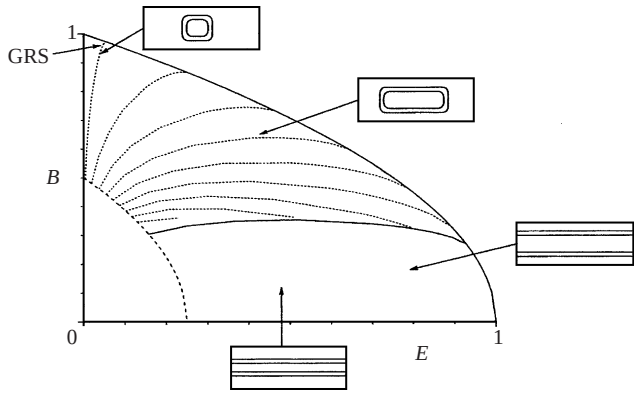

FIGURE 10. Phase diagram of the Gibbs states versus the energy E and the asymmetry parameter B, with quadratic topography and a domain aspect ratio corresponding to the Great Red Spot parameters (400 000 km to 20 000 km). The outer line is the maximum energy achievable for a fixed $B:E = \frac{1}{2}R^2(1-B^2)$. The inner solid line corresponds to the boundary between the vortex and straight jet solutions. The dashed line corresponds to the limit of validity of the small deformation radius hypothesis. It has been drawn using the condition that the maximal vortex width (81) be equal to two Rossby deformation radii. The dotted lines are constant vortex aspect ratio lines with values 2, 10, 20, 30, 40, 50, 70, 80 respectively.

non-dimensional quantity

$$\frac{\sigma^* y_{max}^{*3}}{v_{max}^* l^{*2}} = i(u), \tag{83}$$

with $i(u) \equiv 6e(u)/(uv(u)\sigma(u)l^2(u))$. As may be seen in figure 7(b), the function $i(u)$ is an increasing function of u ranging from 0 to $3/(4\log^2(2))$. Once u is determined from (83), the other parameters are clearly determined by (82).

Let us assume, in contrast, that we know *a priori* the physical parameters, namely the deformation radius R^*, the deep zonal shear (topography a^*), and the forcing conditions ($a_1^* - a_{-1}^*$, asymmetry B and energy E). Then our model predicts the final organization resulting from PV mixing. We can in particular predict the competition between a zonal jet equilibrium and an annular vortex, as represented in the (E, B) diagram of figure 10. This diagram is obtained by first deducing, with the zero-order results (34) and (33), the values of the segregation parameter u and of the area occupied by the vortex A_1. From A_1 and u, using the numerical determination of the vortex area versus d, we obtain the appropriate scaling factor c' and the corresponding value of d (assuming an infinite domain length). Each dotted line in the figure represents a vortex shape with a given aspect ratio. The vortex elongation increases with decreasing asymmetry parameters B, forming a pair of zonal jets when the domain aspect ratio is reached (typically 20 in the region of the Great Red Spot). The 'phase transition' between the vortex and zonal jet solutions is therefore continuous (for infinite domain length). A direct comparison of the entropies (68) for (unbounded) vortex solutions and the zonal jet leads to a preference of the latter below the solid curve in figure 10. This boundary is not relevant here, as the vortex solution no longer exists along this line (the aspect ratio is so large that the vortex is bounded by the domain length). The situation would be however different for a smaller aspect ratio (discontinuous phase transition). The parameters of the Great Red Spot are indicated in the figure. An increase of energy and a decrease of B would yield zonal jets, which may explain what is observed in the northern hemisphere. This

could be physically due to an excitation by a wider convective plume, as discussed in next section.

4. Application to Jupiter's Great Red Spot and Oval BC

We here discuss how our statistical mechanics predictions fit with Jupiter's data. This is not an easy task as key physical parameters are poorly known. Busse (1983) first suggested that the alternating eastward and westward winds observed on Jupiter are generated in the deep interior, and are constant in columns aligned with the axis of rotation. Some authors, however, remark that this is inconsistent with the observed asymmetry of the winds in the southern and northern hemispheres. They propose instead a generation limited to a thin atmospheric layer. Our statistical mechanics approach provides clear predictions for this, see (65): a longitudinally elongated anticyclonic vortex can only persist above maxima of the effective topography $h(y)$, induced by the combined effect of the deep zonal flow and the beta-effect (in the reference frame moving with the structure). Elongated cyclonic vortices must similarly sit on topography minima. Concerning the upper zonal flow, we predict two kinds of flow features in our asymptotic limit of small R: the moderate zonal velocity (66) which reproduces the deep flow structure, but with enhanced velocity, and the stronger velocity in the narrow jets (represented in figure 6) separating subdomains.

Only circular vortices are predicted in the absence of a quadratic beta-effect. In the case of a uniform zonal flow, equivalent to an ordinary (linear) beta-effect, the vortices drift at velocity $-R^*\beta^*$, but remain circular, as discussed in § 3.4. This is specific to the case of small deformation radius. In the opposite limit of the Euler equations, we do obtain elongated vortices in a shear layer as statistical equilibria (Sommeria, Staquet & Robert 1991*b*), even without any beta-effect.

Observations clearly indicate the existence of an intense and narrow jet in the northern hemisphere at 24° N, which dominates the broader zonal flow. The observed asymmetry of the zonal winds in the two hemispheres is mostly due to this intense jet, which has no southern counterpart. The Great Red Spot (GRS) occupies the same latitude region in the southern hemisphere. We claim that the two hemispheres have the same deep zonal flow, while the observed differences correspond to the two kinds of statistical equilibrium solutions in the atmospheric layer (the zonal jets and annular vortex). This could be due to slightly different forcing conditions, as discussed below.

The bottom topography associated with the deep zonal flow has been indirectly determined by Dowling & Ingersoll (1989), from the measured velocity fields in the GRS and White Oval BC, and we can use these data to test our predictions. They analyse the observations in the framework of a 1-1/2 shallow water model (SW), with an active shallow layer floating on a much deeper layer. The SW topography gh_2^*, depending only on the planetographic latitude λ, is then related to the deep layer velocity $v_d^*(\lambda)$ (assumed zonal and steady) by the geostrophic balance $f^* v_d^* = -(1/R_l^*)\,\mathrm{d}(gh_2^*)/\mathrm{d}\lambda$, where g is the reduced gravity and $R_l^*(\lambda)$ the latitudinal planetary radius of curvature. The Bernouilli function $B_e^* = \boldsymbol{v}^{*2}/2 + g(h_1^* + h_2^*)$ and the shallow-water potential vorticity $q_{SW}^* = (\omega^* + f^*)/h_1^*$ (h_1^* is the upper layer thickness) are both advected and thus assumed constant along the streamlines of the steady vortex flow. The field B_e^* is deduced from the observed velocity field $\boldsymbol{v}^*$ (and corresponding vorticity ω^*) by integration of the steady flow relation $\nabla B_e^* = -(\omega^* + f^*)(\boldsymbol{e}_z \times \boldsymbol{v}^*)$. The

topography gh_2^* is deduced from these relations as a quartic fit in the latitude λ:

$$gh_2^* = A_0 + A_1\lambda + A_2\lambda^2 + A_3\lambda^3 + A_4\lambda^4. \tag{84}$$

This fit depends on a single unknown parameter, the Rossby radius of deformation $R^* = \sqrt{gh_0^*}/f_0^*$, where h_0^* is a reference upper layer thickness and f_0^* a reference Coriolis parameter. The same procedure has been applied to both the GRS and the Oval BC, covering different latitude ranges. The coefficients A_i (in the vortex reference frame) are reported in table 1 of Dowling & Ingersoll (1989), for three values of the deformation radius.

Our model is the QG approximation of this shallow water system. Its validity has been discussed by Dowling & Ingersoll (1989) and it was found reasonably good as a first approach, although not accurate. We furthermore use the beta-plane approximation, linearizing the planetary vorticity around a reference latitude λ_0^* (λ_0^* is taken to be $-23°$ for the GRS and $-33.5°$ for the Oval BC). Therefore we write $f^* = f_0^* + \beta^* y^*$, with $f_0^* = 2\Omega^* \sin\lambda_0$ and $\beta^* \equiv 2\Omega^* \cos\lambda_0^*/r_z^*(\lambda_0)$; Ω^* is the planetary angular speed of rotation: $2\pi/\Omega^* = 9\,\mathrm{h}\ 55\,\mathrm{mn}\ 29.7\,\mathrm{s}$ and $r_z^*(\lambda_0)$ is the zonal planetary radius (which slightly differs from the latitudinal radius $R_l^*(\lambda)$ due to the ellipsoidal planetary shape, see formula (4) of Dowling & Ingersoll (1989)). We then obtain the QG potential vorticity (2) with the QG topography $h^*(y^*)$ linked to the SW topography (84) by

$$h^*(y^*) = \frac{gh_2^*}{|f_0^*|R^{*2}} - \beta^* y^*. \tag{85}$$

In our QG model the deep layer zonal flow is given by $v_d^* = R^{*2}(\mathrm{d}/\mathrm{d}y^*)(h^*(y^*) + \beta^* y^*)$ (recall that y^* is directed northward, like λ, and that the Coriolis parameter f_0^* is negative).

We have represented this QG topography (85) in figure 11 for the values of the Rossby deformation radius considered by Dowling & Ingersoll (1989). The result shows that, for both the GRS and the Oval BC, the QG topography has a maximum at a latitude which is nearly the centre of the vortex. It means that the effective beta-effect $\mathrm{d}h^*/\mathrm{d}y^*$ vanishes at this latitude: the planetary beta-effect β^* is balanced by the effect of the sloping interface due to the vertical shear. This means that the bottom velocity $\boldsymbol{v}_d$ is eastward with respect to the atmospheric layer, as can be directly seen in figure 4 of Dowling & Ingersoll (1989).

A quadratic approximation $h^*(y^*) = -a^* R^* y^{*2}$ to the QG topography is indicated in figure 11. It appears to be good for the latitudinal extent of the GRS. Repeating this procedure for the three values $R_1^* = 1700\,\mathrm{km}$, $R_2^* = 2200\,\mathrm{km}$, and $R_3^* = 2600\,\mathrm{km}$, we obtain respectively: $a^* = 5.4 \times 10^{-16}$, 3.3×10^{-16} and $2.5 \times 10^{-16}\,\mathrm{km^{-3}\,s^{-1}}$, corresponding to a deep shear $\sigma_d^* = 0.41 \times 10^{-5}$, 0.70×10^{-5}, and $0.93 \times 10^{-5}\,\mathrm{s^{-1}}$.

The data analysis of Dowling & Ingersoll (1989) also provide the relationship between the SW potential vorticity q_{SW}^* and the Bernoulli function B_e^* in the vortex. This can be translated into a relationship between q_{SW}^* and the SW stream function ψ_{SW}, defined for a steady state by $h_1^* \boldsymbol{v}^* = -\boldsymbol{e}_z \times \nabla\psi_{SW}^*$ (it expresses the conservation of mass $\nabla \cdot (h_1^* \boldsymbol{v}^*) = 0$). From the steady SW equations, $\mathrm{d}B_e^*/\mathrm{d}\psi_{SW}^* = -q_{SW}^*$, so that $\psi_{SW}^*(B^*)$ can be deduced from $q_{SW}^*(B^*)$. We have numerically computed this relation, $\psi_{SW}^* = \int {q_{SW}^*}^{-1}\,\mathrm{d}B^*$ (up to an arbitrary constant for ψ_{SW}^*) from the data of Dowling & Ingersoll (1989). Using that q_{SW}^* and ψ_{SW}^* are respectively proportional to the QG potential vorticity q and stream function ψ in the QG limit, we can compare these curves with our $q(\psi)$ relation. The result, shown in figure 12, is consistent with the tanh predicted for a two-PV-level statistical equilibrium. The maximum and minimum

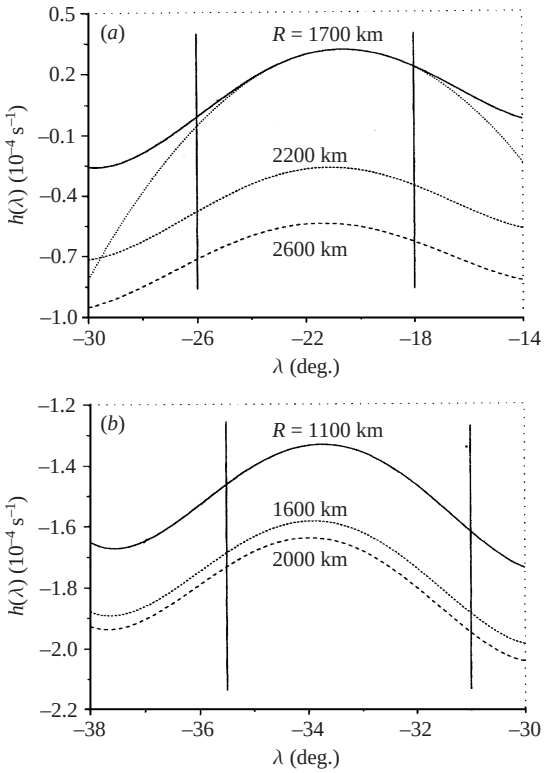

FIGURE 11. QG topography (units s^{-1}) versus latitude computed from data of Dowling & Ingersoll (1989): (*a*) under the GRS; (*b*) under the Oval BC.

values of q^*_{SW} provide an estimate of the corresponding PV levels. Converted to QG variables, this reads $u(a^*_1 - a^*_{-1}) = 0.8$, 0.68, and 0.61 (units $10^{-4}\,s^{-1}$) for $R^* = R^*_1$, R^*_2 and R^*_3 respectively.

These values are consistent with a PV difference of order of the planetary vorticity $|f^*_0| = 1.35\,10^{-4}\,s^{-1}$. A physical justification could be that PV spots with value $-f^*_0$, occupying a small area proportion are randomly generated in the active layer. This could be the result of intense incoming thermal plumes, as recently observed by Ingersoll *et al.* (2000): conservation of the absolute angular momentum during the radial expansion leads to a strong decrease of the local absolute vorticity, which comes close to zero. This means that in the planetary reference frame, a local vorticity patch with value $-f^*_0$ is created. The opposite vorticity is globally created by the subducting flow, but it is close to zero due the much larger area.

We can alternatively deduce the parameters of our model from more direct observations, using (83) and (82). We take the ambient shear $\sigma^* = 1.5\,10^{-5}\,s^{-1}$ from the analysis of Jupiter's zonal flow by Limaye (1986). Mitchell *et al.* (1981) have analysed the GRS jet velocity, assuming an elliptical shape for the vortex, and plotted the tangential velocity with respect to the greater axis length of these ellipses. From this study we take $v^*_{max} = 120\,m\,s^{-1}$. Taking the ellipse greater axis where the velocity achieves its maximum and rescaling it with the ellipse aspect ratio we obtain $y^*_{max} = 4700\,km$. This analysis does not permit a precise determination of the jet width l^*. The first reason is that velocity data in the outside part of the jet are sparse. The second reason is that the width depends on latitude (the jet

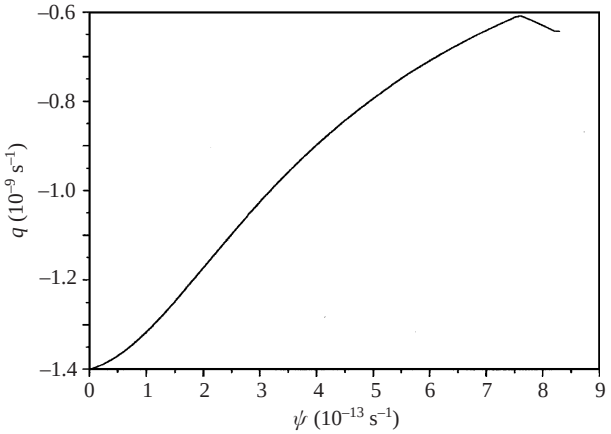

FIGURE 12. Potential vorticity q^*_{SW} versus stream function Ψ^*_{SW} from the determination of $q^*_{SW}(B^*_e)$ by Dowling & Ingersoll (1989) (their table 1) in the Great Red Spot (for $R = 2200\,\mathrm{km}$ $q : 10^{-9}\,\mathrm{s}^{-1}$ and $\Psi : 10^{13}\,\mathrm{m\,s}^{-1}$). These SW potential vorticity and stream function are proportional to the QG ones in the QG limit. We observe that this function is in reasonable agreement with the tanh-like relation of the two-PV-level Gibbs states.

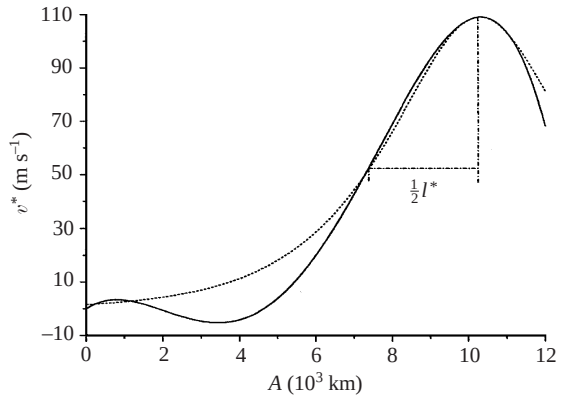

FIGURE 13. Velocity profile within the GRS from Mitchell *et al.* (1981). They have observed that the velocity is nearly tangential to ellipses. Using a grid of concentric ellipses of constant eccentricity, the velocities have been plotted with respect to the semi-major axis $\mathscr{A}$ of the ellipse on which the measurement point lies. Results have been fitted by a quartic in $\mathscr{A}$. l^* is the jet width, defined as the width in which the jet velocity is greater than half the maximum velocity.

has a greater width where the curvature is larger). From the data of Mitchell *et al.* (1981), we deduce that on the ellipse major axis the jet width is 5600 km (see figure 13); following its elliptical approximation, this corresponds to a 2600 km jet width on the minor axis. To fit with our asymptotic analysis, we need to take a (single) value between these two extrema, $3000\,\mathrm{km} \leqslant l^* \leqslant 5000\,\mathrm{km}$. We then use the non-dimensional expression (83) to determine the value of the segregation parameter u and deduce the other free parameters from (82). For $3000\,\mathrm{km} \leqslant l^* \leqslant 5000\,\mathrm{km}$, we obtain $0.92 \leqslant u \leqslant 1$ (u decreases as l^* increases), $1580\,\mathrm{km} \leqslant R^* \leqslant 2000\,\mathrm{km}$ (R^* decreases as l^* increases), $1.2 \times 10^{-4}\,\mathrm{s}^{-1} \leqslant a^*_1 - a^*_{-1} \leqslant 3.1 \times 10^{-4}\,\mathrm{s}^{-1}$ ($a^*_1 - a^*_{-1}$ increases as l^* increases), $9.0 \times 10^{-16}\,\mathrm{km}^{-3}\,\mathrm{s}^{-1} \leqslant a^* \leqslant 1.4 \times 10^{-15}\,\mathrm{km}^{-3}\,\mathrm{s}^{-1}$ (a^* increases as l^* increases) and $1.1 \times 10^{-5}\,\mathrm{s}^{-1} \leqslant \sigma^*_d \leqslant 1.5 \times 10^{-5}\,\mathrm{s}^{-1}$ (σ^*_d increases as l^* increases). We note that this deep shear σ^*_d, deduced from the surface observations with our model,

is in reasonable agreement (within a factor of two) with the analysis of Dowling & Ingersoll (1989).

In this range of values, we note that $a_1^* - a_{-1}^* = |f_0^*|$ is obtained for $l^* = 3200\,\mathrm{km}$, $u = 0.99$, $R^* = 2000\,\mathrm{km}$, $a^* = 9.7 \times 10^{-16}\,\mathrm{km^{-3}\,s^{-1}}$, $\sigma_d^* = 1.5 \times 10^{-5}\,\mathrm{s^{-1}}$. We have chosen these parameters to plot the GRS point in the phase diagram of figure 10. A channel width of 20 000 km has been chosen (but this parameter is not critical as long as the equilibrium vortex is not constrained by the lateral boundaries). The asymmetry parameter B is then obtained from the observed GRS area using (33).

We can predict the effect of changing the forcing parameters B and E in the phase diagram. Slightly larger area (smaller B) and energy lead to more elongated vortices. At the end of the nineteenth century, the GRS was longer (40 000 km) with the same width (Beebe & Youngblood 1979). Our model indeed indicates that the GRS length is sensitive to the forcing parameters (in particular to B, unlike its width y_{max}, strongly constrained by (82)). Elongated vortex solutions also provide a good description of the dark brown cyclonic spots ('Barges') at 14° N on Jupiter, as studied from Voyager observations by Hatzes *et al.* (1981). The measured velocities show a boundary jet organization around the perimeter of the barge ($v_{max}^* = 25\,\mathrm{m\,s^{-1}}$), see figure 1(*b*), in agreement with our model. However the surrounding zonal shear is such that velocity at the maximum latitude of the barge is the same as the maximum jet velocity, so that our approximation $aL_V^2 \ll 1$ is not good. Note that this vortex is cyclonic (in a cyclonic shear), supporting our view that the anticyclonic direction of the GRS is a feature of the forcing condition, rather than a fundamental dynamical constraint.

For still smaller values of B, we obtain an x-independent uniform PV band, bounded by intense zonal jets. There are two jets of opposite direction on each side of the uniform PV band, but this is a peculiarity of the symmetry of this model with respect to the y-coordinate. We may expect that on the half-sphere (e.g. on the northern hemisphere), a single eastward jet can separate a high-PV mixed region in the north from a low-PV mixed region in the south. This could explain the intense westward jet observed at 24° N. According to our model, this could be due to a different convective activity than in the southern hemisphere, generating a more balanced proportion of positive and negative PV patches.

The stability of such an intense jet has been a puzzling problem. We find that a single jet satisfies the usual Fjortjoft condition of barotropic stability: its PV monotonically varies with latitude between the values q_{-1} and q_1. By contrast, for the pair of jets obtained in our channel geometry, there is a PV maximum q_1. This maximum is very flat however, corresponding to the uniform PV region. Numerical simulations indicate that this state is also stable, as we show in a forthcoming publication (the Fjortjoft criterion is only a sufficient condition of stability, not a necessary one). More generally the maximum entropy states are always found to be dynamically stable, although this remarkale result has not been rigorously proven in general.

5. Conclusions

A first achievement of this work is the general analysis of the statistical mechanics equilibrium states for the quasi-geostrophic model, in the limit of small Rossby deformation radius. In the absence of topography or beta-effect, turbulence mixes potential vorticity in subdomains, and jets occur at the interfaces of these subdomains, with a width of the order of the deformation radius. From a thermodynamic point of view, this is like the coexistence of two phases. Indeed, the vortex interaction becomes short ranged in the limit of small deformation radius, and statistical mechanics leads

to a thermodynamic equilibrium between two 'phases', with different concentrations of the potential vorticity levels. The same conclusion is obtained from the general partial differential equation (18) characterizing the equilibrium states. This equation reduces to the algebraic equation (20) in the limit of small deformation radius, and the two uniform subdomains correspond to two solutions ψ_{-1} and ψ_1 of this equation. At the interface of these subdomains, the general partial differential equation (18) reduces to the equation (38), whose solution determines the jet velocity profile. In addition, a solvability condition of this equation confirms the equilibrium relation between the two 'phases', which was obtained in the thermodynamic approach.

Our results are for two initial potential vorticity levels only, to simplify the algebra. However the conclusion that potential vorticity mixes in subdomains separated by intense jets, scaling like the Rossby deformation radius, is quite general. It can also be generalized to the shallow water model, beyond the QG approximation. Any initial distribution of PV levels will lead to a monotonic function $q(\psi)$ reaching asymptotic extrema at the minimum and maximum PV levels (Robert & Sommeria 1991). In most cases such a function will still be represented by a tanh-like curve, corresponding again to the coexistence of two phases as represented in figure 3. We may also imagine a curve with more than one inflection point, instead of a single one, resulting in the coexistence of more than two phases. The most common case will be a two-phase equilibrium however. Likewise in thermodynamics the coexistence of more than two solutal phases is unlikely, even when many chemicals (equivalent to PV levels) are mixed.

In the ocean or Earth's atmosphere, the shallow water model (or its QG approximation) is of limited interest. Indeed, vortices larger than the Rossby radius of deformation may be unstable to baroclinic instability, which is only captured with (at least) a two-layer model. In the limit of a thin upper layer, the growth rate of this instability decreases like the ratio of the upper layer thickness to the lower one, but it never cancels. By contrast the single layer model has no baroclinic instability. Extension of the present statistical mechanics results to a two-layer model would be therefore desirable.

The atmosphere of the Giant Planets is possibly the best field of application of the shallow water model with small radius of deformation: it represents a stratified atmosphere floating on the much deeper convective interior. In this context of shallow water, many models of coherent vortices have been proposed to explain the Great Red Spot of Jupiter. The models of solitary waves (Maxworthy & Redekopp 1976; Petviashvili 1981) address the robustness with respect to the dispersive effect of Rossby waves. They do not, however, explain the robustness amidst turbulent mixing, a stricking feature of spacecraft images. By contrast our maximum-entropy vortex is not destroyed by turbulence: it results instead from the most complete PV mixing consistent with energy conservation. The planetary beta-effect is balanced by the modification of the zonal flow due to PV mixing, suppressing Rossby wave propagation: the coherent vortex does not propagate with respect to the zonal flow at the latitude of its centre, in agreement with observations.

In spite of the approximations (QG with small radius of deformation), our analysis provides specific predictions which can be clearly compared with present or future observations. The annular jet structure of the GRS is explained (unlike in solitary wave theories). We can deduce the radius of deformation to be in the range 1580–2000 km, from the fit of our model to the atmospheric wind data. We find that its elongated shape must be associated with a deep zonal shear, such that the effective beta-effect is quadratic at the latitude of the vortex centre. This means that the deep fluid moves

eastward at the latitude of the GRS centre, at velocity $R^{*2}\beta^* = 12$–$18\,\mathrm{m\,s^{-1}}$. Such a prediction is in agreement with the data analysis of Dowling & Ingersoll (1989). Two vortices trapped at the same latitude tend to merge, as this clearly minimizes the boundary length (like droplet merging by capilarity).

We can provide a general understanding of the organization of atmospheric motion in a Giant Planet, with small radius of deformation. In the absence of a deep zonal flow, we would find only intense zonal jets, with width of order R, or circular vortices, with a circular annular jet structure.

We therefore conclude that the observed eastward and westward jets, much broader than the deformation radius, must be due to a deep zonal flow. This deep shear is reproduced in the atmospheric layer, with an amplifying factor. Furthermore a systematic westward velocity tends to appear, as a consequence of mixing of the planetary PV.

If a local extremum of the topography $h(y)$ is reached, resulting in a quadratic effective beta-effect, an isolated coherent vortex, with longitudinally elongated shape, tends to be trapped. It is cyclonic for a minimum of $h(y)$, corresponding to a cyclonic background shear, and anticyclonic otherwise. The vortex equilibrium is centred on the topography extremum, so it does not depend on the artificial channel boundaries that we have introduced. In a more realistic multi-zone model, similar vortices would appear as local equilibria, which could be meta-stable states of the global system. Note that the latitude of the topography extremum, and the resulting vortex latitude, depend on the chosen reference frame, which is itself set by the x-wise momentum of the system. Depending on this parameter, the vortex can be at any latitude, going with the local zonal flow.

An alternative possibility is the formation of intense zonal jets, scaling like the deformation radius. The choice depends on the energy and initial areas of the PV patches, as demonstrated in figure 10: a forcing by larger PV patches, resulting from a stronger convective activity, could lead to a zonal jet.

For a more explicit application to the Giant Planets, a model of forcing should be combined with our statistical mechanics approach. Forcing by incoming convective plumes is a good candidate, as it produces a small area of high anticyclonic vorticity, with value of order $-f$. Another possibility could be baroclinic instability, as produced by Read & Hide (1984) in a laboratory experiment. They have obtained a single coherent vortex in a rotating annulus with internal heating and cooling at the sides. Interestingly, the corresponding geostrophic flow tilts the isopycnals with a maximum at the centre of the annular channel, like with our topography.

In practice, the forcing should be introduced in kinetic equations like those developed in Kazantsev *et al.* (1998): the local PV fluctuations would be controlled by a balance between local forcing and cascade process toward small scales, in addition to the horizontal mixing described by the present statistical theory. The eddy diffusivity depends on the scale of the fluctuations, but not the resulting equilibrium, which only depends on the probability distribution of the PV levels (which can be conveniently sketched in a model with only two levels). Furthermore, if we completely smooth out the local fluctuations of a statistical equilibrium, then entropy maximization, taking the new initial PV distribution, yields again the same equilibrium structure (Robert & Sommeria 1991). Therefore our equilibrium model provides a robust description of the mean flow, while the local fluctuations are strongly influenced by the forcing and cascade effect.

Improvements of our equilibrium model could be made along the following lines. First the approximation $R \ll r$ of a thin jet, convenient for a qualitative understanding

via analytically tractable computation, is only marginally satisfied. Moreover we have used a model quadratic topography and treated it as a first-order perturbation, which in view of Dowling & Ingersoll (1989) data is not valid in the outer region of the GRS. These limitations can be overcome by numerical determination of the Gibbs state (18) using the relaxation methods of Turkington & Whitaker (1996) or Robert & Sommeria (1992). Furthermore, extension to the more general shallow water model is desirable, as the Rossby number ($\simeq 0.36$ where it is maximal) is not very small. The corresponding formulation has been given by Chavanis & Sommeria (2000).

Of course the whole approach relies on the assumption that potential vorticity mixing is only constrained by the conservation laws. The underlying idea of potential vorticity mixing by geostrophic turbulence has been proved relevant in oceanic gyres (Rhines & Holland 1979). In the case of the Euler equations, some numerical and laboratory experiments quantitatively support this statistical mechanics approach: it describes well the result of vortex merging. In other cases mixing may not be global but restricted to active regions (see e.g. Sommeria 2001). Organization into local vortices, rather than at the scale of the whole domain, is more likely with a small radius of deformation, as vortex interactions leading to coalescence are then screened. This is observed for instance in the numerical computations of Kukharkin & Orszag (1996). By contrast, the zonal shear in the Giant Planets promotes vortex encounters, due to the latitude shift induced by vortex interaction. We therefore expect a good relaxation toward the global statistical equilibrium in the shear zone domain considered, always involving a single vortex. A good illustration of mixing properties is given by the White Ovals. Three Ovals have persisted since their discovery in 1938, at an equidistant position about 120° apart in longitude (see Beebe & Youngblood 1979). Within the last three years, these vortices have formed a single one by two successive merging events. Such merging is predicted by statistical mechanics. However the equidistant position is mechanically stable and the system only slowly moves away from it by the effect of turbulent fluctuations. Similar behaviour has been observed in a rotating tank experiment (Meyers, Sommeria & Swinney 1989).

The authors thank R. Robert for collaboration on statistical mechanics approach and for useful comments on the present work.

Appendix A. Axisymmetric equilibrium vortices

We have noted in § 2.3.1 that, when for instance $B > 0$, in the limit of small energy ($E \to 0$ or equivalently $u \to |B|$, for fixed B and R), the area A_{-1} occupied by ψ_{-1} tends to 1, the whole domain. Therefore, in this limit, the complementary area A_1 tends to 0 and the vortex becomes smaller than the deformation radius, so we can no longer neglect the curvature radius of the jet.

In this limit $u \to |B|$, as the vortex has a small area with respect to the total domain it is not affected by the boundary conditions, so it can be supposed axisymmetric. We introduce the rescaled stream function

$$\phi = -\frac{\alpha}{C} + \frac{\psi}{R^2}, \tag{A 1}$$

which depends only on the radius r (expressed in units of the Rossby radius R). From the general Gibbs state equation (18), we then deduce the axisymmetric vortex equation:

$$-\frac{\mathrm{d}^2\phi}{\mathrm{d}r^2} - \frac{1}{r}\frac{\mathrm{d}\phi}{\mathrm{d}r} = -\phi - \frac{\alpha}{C} + B + \tanh(C\phi). \tag{A 2}$$

From now on, we shall consider the case $B > 0$ (the case $B < 0$ is just the symmetric case of a negative vortex).

For this equation to describe a localized vortex, we impose $\lim_{r\to\infty} \phi(r) = \phi_{-1} \equiv -\alpha/C + \psi_{-1}/R^2$, where ψ_{-1} is the positive solution of the algebraic equation (20). Since nearly the whole fluid domain is covered by the asymptotic stream function ψ_{-1} outside the vortex, the condition of zero total circulation $\langle q\rangle = \langle\psi\rangle/R^2 = 0$ imposes that $\psi_{-1} \simeq 0$ (it is of order R), so that $\phi_{-1} = -\alpha/C$, and the algebraic equation (20) then leads to

$$\alpha = \arg\tanh(B). \tag{A 3}$$

We can thus eliminate α in (A 2), leading to an equation depending on two parameters, B and C, with boundary conditions

$$\frac{\mathrm{d}\phi}{\mathrm{d}r}(r=0) = 0 \quad \text{and} \quad \lim_{r\to\infty} \phi(r) = -\frac{\arg\tanh B}{C}, \tag{A 4}$$

where the regularity condition at $r = 0$ has been included.

Let us consider, as in § 2.3.2, the analogy of equation (A 4) with one-particle motion with 'position' ϕ and 'time' r. The right-hand side of (A 2) can be written as the derivative $-\mathrm{d}U/\mathrm{d}\phi$ of the potential,

$$U(\phi) = \frac{\ln(\cosh(C\phi))}{C} - \frac{\phi^2}{2} + \left(B - \frac{\arg\tanh B}{C}\right)\phi, \tag{A 5}$$

while the first term can be interpreted as a friction effect. Indeed, integration of (A 4) leads to

$$U(\phi_{-1}) - U(\phi(r=0)) = -\int_0^{+\infty} \frac{1}{r}\left(\frac{\mathrm{d}\phi}{\mathrm{d}r}\right)^2 \mathrm{d}r < 0. \tag{A 6}$$

Thus, in figure 3(*a*), the hatched area on the right must be greater than the one on the left (since $(U(\phi_1) - U(\phi_{-1})) > U(\phi(r=0) - U(\phi_{-1}) > 0$). It is clear from this figure that this is possible only if $\phi_0 < 0$ and $\alpha/C < B$, or, using (A 3), $C > \alpha/B = \arg\tanh B/B$. $C = \alpha/B$ corresponds to the integrability condition (41) when the effect of jet curvature is neglected. This effect is now taken into account by the departure of C from this value, which we shall denote $\Delta C \equiv C - \arg\tanh B/B$. Then $\Delta C > 0$ and we expect to recover the results of § 2.3.2 in the limit $\Delta C \to 0$. Moreover, we must reach a uniform stream function at large distance, the solution of the algebraic equation (20), so it must have three solutions. We easily show that the corresponding ΔC must not exceed a maximal value, denoted ΔC_{max}.

We can prove that for any $B > 0$ and $\arg\tanh B/B < C < \arg\tanh B/B + \Delta C_{max}$, equation (A 4) has a unique solution. Such solutions have been numerically obtained for $B = 0.75$ and $0 < \Delta C < \Delta C_{max}$. Corresponding stream function profiles are shown in figure 14.

As ΔC is decreased from ΔC_{max} to zero, two stages can be seen in figure 14. First the maximum value of the stream function is increased while the mean width of the vortex remains of the order of R. In a second stage, when ΔC goes to zero, as we are closer to the integrability condition for big vortices (41), ϕ remains longer in the vicinity of ϕ_1 so the vortex size increases. Note that the energy monotonically increases as ΔC is decreased, first by an increase in the vortex maximum stream function and then by an increase in size. Finally the case of a jet with negligible curvature studied in § 2.3.2 is reached when $\Delta C \to 0$.

In conclusion, we have shown that in the limit of small energy, with fixed B and R, the Gibbs states are approximated by axisymmetric vortices, whose radial structure

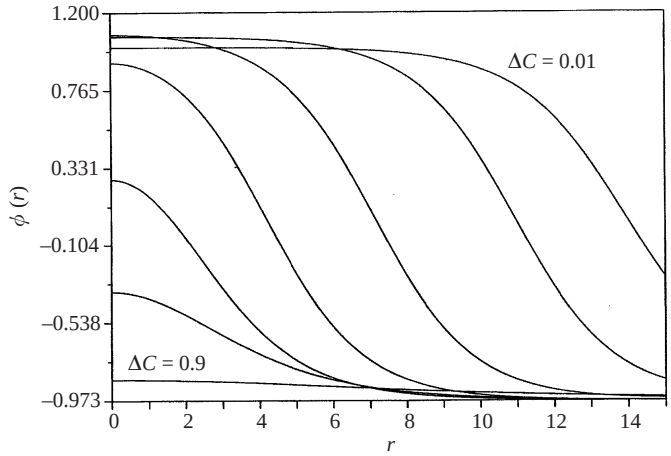

FIGURE 14. Various axisymmetric stream-function profiles for decreasing ΔC (ΔC = [0.9, 0.6, 0.3, 0.1, 0.05, 0.03, 0.01] and $B = 0.75$). The non-dimensional stream function ϕ is plotted versus the radius, normalized by the Rossby deformation radius.

depends on the parameter ΔC, which monotonically decreases from ΔC_{max} to 0 as energy is increased.

Appendix B. Determination of the Gibbs state by direct entropy maximization, in the presence of a topography (beta-effect)

In § 3.3, we studied the limit of small Rossby deformation radius in the Gibbs state equation (51) by considering the jet equation (55) and its integrability condition (60). We deduced that the Gibbs states are composed of subdomains in which ψ satisfies the algebraic equation (54) separated by an interfacial jet whose curvature satisfies (65). The aim of this Appendix is to prove that these results can be obtained by directly maximizing the entropy, adapting the method used in § 2.3.1.

Let us make the following assumptions:

1. In the limit of small Rossby deformation radius, the probability p of finding the PV level a_1 takes two values $p_{\pm 1}(y)$, depending only on y. We are looking for vortex solutions. The vortex shape is described by the length $\Lambda(y)$ on which the probability p takes the value $p_{-1}(y)$ (see figure 15).

2. The two subdomains where p take the two values $p_{\pm 1}(y)$ are separated by a jet. The probabilities $p_{\pm 1}(y)$ are supposed to be close to their values without topography $p_{\pm 1} = \pm u$, such that the free energy per unit length of the jet is approximated well by that calculated without topography (44). If L_V denotes the vortex size, $1/\sqrt{a}$ a typical length on which topography varies, we will show this approximation to be valid as long as $aL_V^2 \ll 1$.

3. The boundary conditions can be relaxed; that is no boundary term appears in the variation of the free energy at the order considered here (see the discussion concerning boundary jets in § 3.3).

Given these, the Gibbs state is described by the three functions $p_{\pm 1}(y)$ and $\Lambda(y)$. We will determine them by maximizing the entropy S (15) under the three constraints: energy (48), mass conservation (46) and momentum (49). A necessary condition for a solution to this variational problem is the existence of three Lagrange parameters

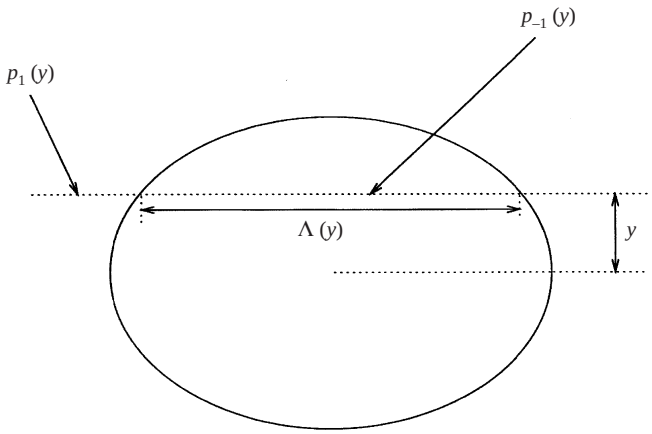

FIGURE 15. Definition of $\Lambda(y)$.

C_0, α_0 and γ such that the first variations of the free energy

$$F \equiv -S - \frac{C_0}{R^2}E + \alpha_0 \frac{\langle \psi \rangle}{R^2} + \gamma M \tag{B 1}$$

vanish. Using (15), (48), (46) and (49) together with (2) and (11) and the above assumption (see figure 15), a direct calculation shows that the free energy (B 1) is, up to a constant,

$$F = \int_{y_{min}}^{y_{max}} [f(p_1(y), y)(1 - \Lambda(y)) + f(p_{-1}(y), y)\Lambda(y)] \, \mathrm{d}y (p - \tfrac{1}{2})$$

$$+ \int_{-1/2}^{y_{min}} f(p_1(y), y) \, \mathrm{d}y + \int_{y_{max}}^{1/2} f(p_1(y), y) \, \mathrm{d}y + LF_{Jet}(u) \tag{B 2}$$

with

$$f(p, y) \equiv (p \log p + (1 - p) \log(1 - p)) - 2C_0(p - \tfrac{1}{2})^2 - 2(C_0 B - \alpha_0)(p - \tfrac{1}{2})$$
$$-2(C_0 h(y) - \gamma y)$$

and where L is the jet length, $F_{Jet}(u)$ is the jet free energy per unit length (44), calculated without topography.

Considering first variations of the free energy (B 2) under variations of $p_1(y)$ (resp. $p_{-1}(y)$) proves that $(\partial f / \partial p)(p_1(y), y) = 0$ and that $(\partial f / \partial p)(p_{-1}(y), y) = 0$. A direct calculation shows that

$$2(p_{\pm 1} - \tfrac{1}{2}) = \tanh(2C_0(p_{\pm 1} - \tfrac{1}{2}) + C_0 h(y) - \gamma y + C_0 B - \alpha). \tag{B 3}$$

Using (11) and (2) and recalling that we neglect the Laplacian term, a straight calculation shows that (B 3) is equivalent to the algebraic equation (54).

Let us consider now first variations of the free energy (B 2) under small variations

$\delta\Lambda(y)$ of $\Lambda(y)$. Using that the length of the jet is given by

$$L = 2\int_{y_{min}}^{y_{max}} \sqrt{1+\tfrac{1}{4}(\mathrm{d}\Lambda/\mathrm{d}y)^2}\,\mathrm{d}y,$$

a straightforward calculation shows that

$$\delta L = -\int_{y_{min}}^{y_{max}} \delta\Lambda(y)/r\,\mathrm{d}y$$

where r is the radius of curvature of the jet. We thus deduce from first variations of the free energy (B 2) that

$$\frac{F_{Jet}(u)}{r} = f(p_1(y),y) - f(p_{-1}(y),y). \tag{B 4}$$

From assumption 2 $aL_V^2 \ll 1$ permitted us to consider $F_{Jet}(u)$ as independent of y. In accordance with this hypothesis we evaluate $f(p_1(y),y)-f(p_{-1}(y),y)$ at order zero, with $p_{\pm1} = \frac{1}{2}(1\pm u)$ at this order. We obtain $f(p_1(y),y)-f(p_{-1}(y),y) = 2u(\alpha_1 + C_0 h(y) - \gamma y)$. Moreover using the free energy per unit length expressions (44), (39) and (40), one can show that $F_{Jet}(u) = 2e(u)C_0R$ where $e(u)$ is defined by (64). These two last results show that (B 5) is equivalent to (65), the expression for the radius of curvature r found by the integrability condition for the jet.

Appendix C. Conditions for closed-jet (vortex) solutions of equations (77), (79) and (78) of the oval-shaped vortex boundary

We here investigate in which cases equations (78), (79) with $d > 0$, defining the curve followed by the jet, admit periodic solutions both in x and y, corresponding to vortices. As stressed in § 3.5, equations (78) derive from the Hamiltonian (80), in which y and θ are the two conjugated variables. Let us study the phase portrait of H. For θ in $[0, 2\pi[$, there are four critical points: $P_1 = (0, 1/\sqrt{d})$, $P_2 = (0, -1/\sqrt{d})$, $P_3 = (\pi, 1/\sqrt{d})$, $P_4 = (\pi, -1/\sqrt{d})$. By linearization around these fixed points, one can easily prove that P_1 and P_4 are stable fixed points whereas P_2 and P_3 are hyperbolic fixed points. This permits us to draw the phase portraits of figure 16. Using the expression (80) for H, we obtain that the unstable manifolds are given by $1 - 2/(3\sqrt{d}) = H$ and $-1 + 2/(3\sqrt{d}) = H$ respectively. The parameter d governs a transition of the phase-space structure, from figures 16(a) to 16(b). This transition occurs when the two unstable manifolds merge, for $d = \frac{4}{9}$.

We are looking for vortex solutions of (78), (79), for which the jet angle θ must monotonically depend on the coordinate s, without bound. This excludes the closed curves (c) in figure 16 (which would correspond to oscillating jet solutions). Furthermore, a single position y must be reached for each angle θ, which excludes the curves b2 of figure 16(b) (these would lead loops in the physical space).

Another condition for closed jets is that x, determined by (79), must be a periodic function of θ. We can show that this is only possible for $H = 0$. Indeed, let us denote by Δx the x variation when θ is in $[0, 2\pi]$. We thus impose the condition $\Delta x = 0$. Using (79) and (78) we calculate

$$\begin{aligned}\Delta x &= \int_0^L \cos\theta\,\mathrm{d}s = \int_0^{2\pi} \frac{\cos\theta\,\mathrm{d}\theta}{-dy^2(\theta)+1} \\ &= \int_{-\pi/2}^{\pi/2} \cos\theta \frac{d[y^2(\theta) - y^2(\theta-\pi)]}{(-dy^2(\theta)+1)(-dy^2(\theta-\pi)+1)}\,\mathrm{d}\theta = 0.\end{aligned} \tag{C 1}$$

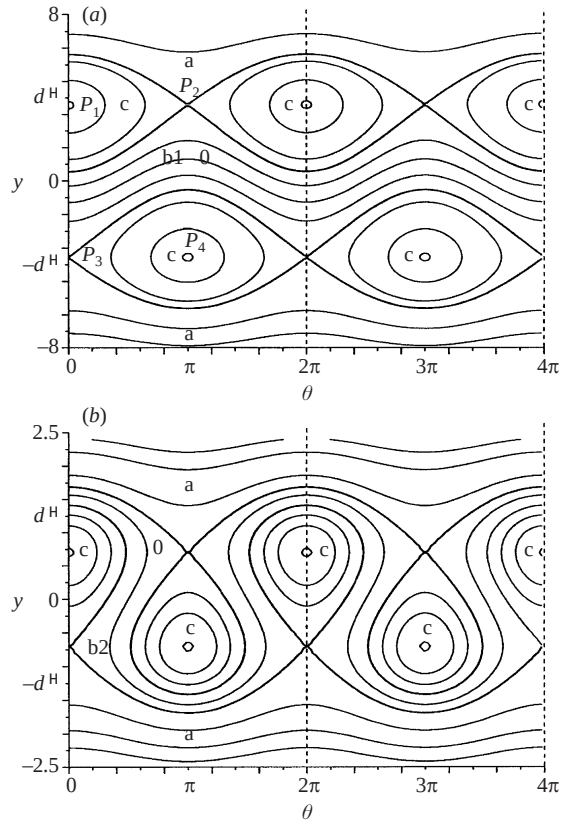

FIGURE 16. Phase portraits of the Hamiltonian H (80) for $y_0 = 0$, governing the jet shape via differential equations (78) (two periods in θ). For vortices, we are looking for periodic solutions in y. Thus only trajectories a and b are of interest. Conversely the closed trajectories c could correspond to oscillating jets. The parameter d governs a transition between two types of phase portraits. (a) For $d < \frac{4}{9}$ (here $d = 0.075$), only the trajectory labelled 0 represents a vortex. (b) For $d > \frac{4}{9}$ (here $d = 2$, the curves $y(\theta)$) admit double points, so they cannot define a vortex.

(The last expression is obtained rewriting the integral as a sum on $[-\frac{1}{2}\pi, \frac{1}{2}\pi]$ plus a sum on $[\frac{1}{2}\pi, \frac{3}{2}\pi]$ and performing a change of variables.) Let us study the sign of $y^2(\theta) - y^2(\theta - \pi)$. Using (80) we deduce that $-d(y^3(\theta)/3) + y(\theta) = H - \cos\theta$ and $-d(y^3(\theta - \pi)/3) + y(\theta - \pi) = H + \cos\theta$. From these two relations we conclude that $y(\theta - \pi) = y(\theta)$ implies $\cos(\theta) = 0$ and that $y(\theta - \pi) = -y(\theta)$ implies $H = 0$. Thus if $H \neq 0$, $y^2(\theta) - y^2(\theta - \pi)$ does not change sign in $[-\frac{1}{2}\pi, \frac{1}{2}\pi]$. Moreover, on the curves a and b1 $(-dy^2(\theta) + 1)$ does not change sign. Thus if $H \neq 0$, the argument of the last integral of (C 1) does not change sign and Δx cannot be zero. We thus conclude that the only solution where x is a periodic function of θ corresponds to $H = 0$.

This solution is the one obtained from (78), (79) with initial conditions $y(0) = 0$ and $\theta(0) = \frac{1}{2}\pi$. Since we have previously excluded the curves b2 (when $d > \frac{4}{9}$) we conclude that no vortex solution exists when $d > \frac{4}{9}$. We conclude that equations (78), (79) with $d > 0$, define a vortex only when $d < d_{max} = \frac{4}{9}$. This solution corresponds to $H = 0$ (80). The vortex then admits a latitudinal and a zonal axis of symmetry.

REFERENCES

Beebe, R. F. & Youngblood, L. A. 1979 Pre-Voyager velocities, accelerations and shrinkage rates of jovian cloud features. *Nature* **280**, 771–772.

Busse, F. H. 1983 A model of mean zonal flows in the major planets. *Geophys. Astrophys. Fluid Dyn.* **23**, 153–174.

Chavanis, P. H. 1998 From Jupiter's great red spot to the structure of galaxies: statistical mechanics of two-dimensional vortices and stellar systems. *Ann. NY Acad. Sci.* **867**, 120–141.

Chavanis, P. H. & Sommeria, J. 1996 Classification of self-organized vortices in two-dimensional turbulence: the case of a bounded domain. *J. Fluid Mech.* **334**, 267–297.

Chavanis, P. H. & Sommeria, J. 2002 Statistical mechanics of the shallow water system. *Phys. Rev.* E **65**, 026302.

Chavanis, P. H., Sommeria, J. & Robert, R. 1996 Statistical mechanics of two-dimensional vortices and collisionless stellar systems. *Astrophys. J.* **471**, 385–399.

Chen, P. & Cross, M. C. 1996 Mean field equilibria of single coherent vortices. *Phys. Rev.* E **54**, 6356–6363.

Dowling, T. E. 1995 Dynamics of Jovian atmospheres. *Annu. Rev. Fluid Mech.* **27**, 293–334.

Dowling, T. E. & Ingersoll, A. P. 1988 Potential vorticity and layer thickness variations in the flow around Jupiter's Great Red Spot and White Oval BC. *J. Atmos. Sci.* **45**, 1380–1396.

Dowling, T. E. & Ingersoll, A. P. 1989 Jupiter's Great Red Spot as a shallow water system. *J. Atmos. Sci.* **46**, 3256–3278.

Hatzes, A., Wenkert, D. D., Ingersoll, A. P. & Danielson, G. E. 1981 Oscillations and velocity structure of a long-lived cyclonic spot. *J. Geophys. Res.* **86**, 8745–8749.

Ingersoll, A. P., Gierasch, P. J., Banfiel, D., Vasavada, A. R. and the Galileo Imaging Team 2000 Moist convection as an energy source for the large-scale motions in Jupiter's atmosphere. *Nature* **403**, 630–632.

Joyce, G. & Montgomery, D. 1973 Negative temperature states for the two-dimensional guiding center plasma. *J. Plasma Phys.* **10**, 107–121.

Kazantzev, E., Sommeria, J. & Verron, J. 1998 Subgridscale eddy parameterization by statistical mechanics in a barotropic ocean model. *J. Phys. Oceanogr.* **28**, 1017–1042.

Kukharkin, N. & Orszag, S. A. 1996 Generation and structure of Rossby vortices in rotating fluids. *Phys. Rev.* E **54**, 4524–4527.

Kuz'min, G. A. 1982 Statistical mechanics of the organization into two-dimensional coherent structures. In *Structural Turbulence* (ed. M. A. Golgshtik), pp. 103–114. Acad. Naouk CCCP Novosibirsk, Institute of Thermophysics.

Limaye, S. S. 1986 Jupiter: new estimates of the mean zonal flow at the cloud level. *Icarus* **65**, 335–352.

Marcus, P. S. 1993 Jupiter's Great Red Spot and other vortices. *Annu. Rev. Astron. Astrophys.* **31**, 523–573.

Maxworthy, T. 1984 The dynamics of a high-speed Jovian jet. *Planet. Space Sci.* **32**, 1053–1058.

Maxworthy, T. & Redekopp, L. 1976 A solitary wave theory of the Great Red Spot and other observed features in the Jovian atmosphere. *Icarus* **29**, 261–271.

Meyers, S. D., Sommeria, J. & Swinney, H. L. 1989 Laboratory study of the dynamics of jovian-type vortices. *Physica* D **37**, 515–530.

Michel, J. & Robert, R. 1994*a* Statistical mechanical theory of the great red spot of Jupiter. *J. Phys. Statist.* **77**, 645–666.

Michel, J. & Robert, R. 1994*b* Large deviations for Young measures and statistical mechanics of infinite dimensional dynamical systems with conservation law. *Commun. Math. Phys.* **159**, 195–215.

Miller, J. 1990 Statistical mechanics of Euler's equation in two dimensions. *Phys. Rev. Lett.* **65**, 2137.

Miller, J., Weichman, P. B. & Cross, M. C. 1992 Statistical mechanics, Euler's equation, and Jupiter's Red Spot. *Phys. Rev.* A **45**, 2328–2359.

Mitchell, J. L., Beebe, R. F., Ingersoll, A. P. & Garneau, G. W. 1981 Flow fields within Jupiter's Great Red Spot and White Oval BC. *J. Geophys. Res.* **86**, 8751–8757.

Modica, L. 1987 Gradient theory of phase transitions and minimal interface criteria. *Arch. Rat. Mech. Anal.* **98**, 123–142.

Onsager, L. 1949 Statistical hydrodynamics. *Nuovo Cimento Suppl.* **6**, 279.

Pedlosky, J. 1987 *Geophysical Fluid Dynamics*, Second Edn. Springer.

Petviashvili V. I. 1981 Red Spot of Jupiter and the drift soliton in a plasma. *JETP Lett.* **32** (11), 619–622.

Read, P. L. & Hide, R. 1984 An isolated baroclinic eddy as a laboratory analogue of the Great Red Spot on Jupiter. *Nature* **308**, 45–48.

Rhines, P. B. & Holland, W. R. 1979 A theoretical discussion of eddy-driven mean flows. *Dyn. Atmos. Oceans* **3**, 289–325.

Robert, R. 1990 Etat d'équilibre statistique pour l'écoulement bidimensionnel d'un fluide parfait. *C. R. Acad. Sci. Paris* **311** (I), 575–578.

Robert, R. 2000 On the statistical mechanics of 2D Euler and 3D Vlasov Poisson equations. *Commun. Math. Phys.* **212**, 245–256.

Robert, R. & Rosier, C. 1997 The modeling of small scales in 2D turbulent flows: a statistical mechanics approach. *J. Statist. Phys.* **86**, 481–515.

Robert, R. & Sommeria, J. 1991 Statistical equilibrium states for two-dimensional flows. *J. Fluid Mech.* **229**, 291–310.

Robert, R. & Sommeria, J. 1992 Relaxation towards a statistical equilibrium state in two-dimensional perfect fluid dynamics. *Phys. Rev. Lett.* **69**, 2776–2779.

Salmon, R. 1988 Hamiltonian fluid mechanics. *Annu. Rev. Fluid Mech.* **20**, 225–256.

Shepherd, T. G. 1990 Symmetries, conservation laws, and Hamiltonian structure in geophysical fluid dynamics. *Adv. Geophys.* **32**, 287–338.

Sommeria, J. 2001 Two-dimensional turbulence. In *New Trends In Turbulence* (Les Houches 2000) (ed. M. Lesieur, A. Yaglom & F. David). EDP/Springer.

Sommeria, J., Nore, C., Dumont, T. & Robert, R. 1991*a* Théorie statistique de la Tache Rouge de Jupiter. *C.R. Acad. Sci.* **312** (II), 999–1005.

Sommeria, J., Staquet, C. & Robert, R. 1991*b* Final equilibrium state of a two dimensional shear layer. *J. Fluid Mech.* **233**, 661–689.

Turkington, B. & Whitaker, N. 1996 Statistical equilibrium computations of coherent structures in turbulent shear layers. *SIAM J. Sci. Comput.* **17**, 1414.